CARL
VON
OSSIETZKY
universität OLDENBURG

Investigation of the deposition method's influence on the layered structure of organic light-emitting diodes

Von der

Fakultät für Mathematik und Naturwissenschaften

der

Carl von Ossietzky Universität Oldenburg

zur Erlangung des Grades und Titels eines

Doctor rerum naturalium (Dr. rer. nat.)

angenommene Dissertation

von

Angelika Maderitsch

geboren am 17.02.1983 in Wien

Gutachter:

Prof. Dr. Jürgen Parisi (Universität Oldenburg)
Prof. Dr. Michael Wark (Universität Oldenburg)

Tag der Disputation: 14.10.2019

Abstract

Organic light-emitting diodes (OLEDs) have a wide variety of technical applications such as bright displays and solid state lighting. An important field of development is the improvement of solution-based deposition techniques. Especially ink-jet printing promises an easy and cost-efficient manufacturing process on large scales. The most efficient OLEDs are multilayer devices, however fabrication of those multilayer structures using solution-based deposition methods is more challenging.

To investigate the influence of the deposition method on the layer structure, simplified model devices were studied. A small molecule host material containing sulfur (S), which was either vapor deposited or solution processed, forms the emission layer (EML). For all investigated samples the hole transport layer (HTL) was solution processed and the electron transport layer (ETL) vapor deposited. In order to gain access to the devices' cross section wedge shaped, electron transparent lamellas were prepared by focused ion beam (FIB) milling. The structure of these samples was investigated using transmission electron microscopy (TEM) and spatially resolved energy dispersive X-ray spectroscopy (EDX). The spatial distribution of S was compared for samples with differently prepared host layers. A significant amount of S could be detected in the HTL beneath the solution processed host layer.

Differently prepared single and multilayer samples were also investigated with a grazing incidence X-ray fluorescence (GIXRF)/X-ray reflectometry (XRR) approach. These measurements fortified the previous result, that S could only be detected beneath the solution processed host and also provided additional information such as film density and surface/interface roughness. The obtained results also demonstrate that the combination of GIXRF and XRR is a suitable nondestructive analysis method for the characterization of organic thin films with little to no sample preparation required.

Kurzfassung

Organische Leuchtdioden (OLEDs) können für verschiedene Anwendungen eingesetzt werden, wie beispielsweise Displays oder Beleuchtungspaneele. Ein wichtiges Forschungsgebiet ist die Verbesserung von löslich prozessierten OLEDs. Besonders Tintenstrahldruckverfahren versprechen eine einfache und kostengünstige Herstellung großflächiger Elemente. Effiziente OLEDs bestehen aus mehreren Schichten. Die Herstellung löslich prozessierter Mehrschichtsysteme ist herausfordernd.

Um den Einfluss der Herstellungsmethode auf das Schichtsystem zu untersuchen, wurden vereinfachte Modellsysteme gefertigt. Ein Schwefel basiertes Hostmaterial, welches löslich prozessiert oder aufgedampft werden kann, bildet die Emissionsschicht. Für alle Proben wurde die Lochtransportschicht löslich prozessiert und die Elektronentransportschicht aufgedampft. Keilförmige Querschnitte des Mehrschichtsystems wurden mit Hilfe eines fokussierten Ionenstrahls hergestellt. Die Struktur dieser Proben wurde mit einem Transmissionselektronenmikroskop (TEM) und energiedispersiver Röntgenspektroskopie untersucht. Obwohl nur das Hostmaterial Schwefel enthielt, konnte unterhalb der flüssig prozessierten Hostschicht Schwefel auch in der Lochtransportschicht nachgewiesen werden.

Einzel- und Mehrschichtproben wurden mit Röntgenfluoreszenzanalyse unter streifendem Einfall (GIXRF) in Kombination mit Röntgenreflektometrie (XRR) untersucht. Diese Messungen bestätigten die Ergebnisse der TEM-Untersuchungen und lieferten zusätzlich Information zu Schichtdichten, Oberflächen- und Grenzflächenrauhigkeit. Die gewonnen Ergebnisse zeigen, dass die Kombination von GIXRF und XRR auch zur zerstörungsfreien Analyse organischer Mehrschichtsysteme geeignet ist, mit geringen Aufwand zur Probenvorbereitung.

Contents

1 Introduction

Organic light-emitting diodes (OLEDs) attract research interest as they promise a wide variety of application possibilities for displays [1–3] and lighting [4–6]. Some key advantages of OLEDs are a wide viewing angle, fast response time and a low power consumption. As OLEDs show self emission, there is no need for a backlight as used for light-emitting diodes (LEDs), which reduces power consumption and leads to better contrast in regard to the depiction of the color black in displays. OLED devices can be fabricated flat and lightweight. Even transparent and flexible devices are possible [7–10]. Today OLEDs are already used in mobile devices such as smart phones or smart watches and in large displays for television and lighting panels [11,12].

The working principle of OLEDs is based on electroluminescence (EL), which is the emission of light from a material in response to an electric field. It was first reported for an organic material in 1953 by Bernanose [13]. In 1963 Pope et al. [14] reported EL in anthracene single crystals. As organic crystals are brittle, their thickness needed to be between 10 µm to 20 µm. Such thick crystals need a voltage of more than 400 V to observe EL. These high voltage requirements are not suitable for consumer application. The research interest switched from organic crystals to amorphous films, which could potentially be more suited for practical applications. In 1987 Tang and Van Slyke could demonstrate EL from a bilayer device with an operating voltage of below 10 V [15]. The low voltage was achievable as the organic layers had a much smaller thickness of below 150 nm. The first OLED based on solution processable organic polymers was presented by Burroughes et al. in 1990 [16].

A wide variety of different materials and device structures has been investigated since [17, 18]. Improvements of OLEDs in regard to efficiency and life time were achieved by a number of different approaches. Examples are the use of multiple layers with specialized functions to increase EL [1, 12] or phosphorescent emitters to overcome limitation due to the excitons' spin statistics [19]. Best efficiency values are obtained with multilayer vapor deposited devices. For large scale applications and patterned structures, solution processing such as ink-jet printing promises an easier and more cost efficient manufacturing process.

When comparing solution processed OLEDs with vapor deposited devices, significant differences in life time and efficiency are observed [20–22]. Several mechanisms, which could influence the devices' operating parameters were proposed, for example intermixing at material interfaces [23] or lower film density of solution processed layers [20].

The main focus of this work was the analysis of the layered structure of differently prepared organic layer stacks. A sulfur (S) based small molecule (SM) host material, which can be either vapor deposited or solution processed was chosen. Different analytical techniques were used to investigate samples. First, a well established method, TEM-EDX on samples prepared using FIB milling, was used to get the spatial distribution of S within the cross section of the layer stack. Furthermore, a combined grazing incidence X-ray fluorescence (GIXRF)/X-ray reflectometry (XRR) approach was investigated. This analytical technique, which is not well established when investigating organic thin films, promises similar information, such as film thickness or element distribution, with much simpler sample preparation. In addition, data about surface and interface roughness can also be obtained. It could be shown that this novel approach is very promising for the analysis of organic thin films. Significant differences in the element distribution between solution processed and vapor deposited samples could be shown. The results of both methods were in good agreement. X-ray photoelectron spectroscopy (XPS) measurements provided information on the chemical binding state of S in emission layer (EML) and hole transport layer (HTL).

Following this introduction, the next chapter gives a short overview of organic semiconductor physics and organic light emitting diodes. A brief survey of the analytical methods used are presented in the third chapter of this work. The forth chapter describes in detail sample preparation procedures as well as the analytical setups used. Results are presented and discussed in the fifth chapter. The final chapter summarizes results and conclusions drawn.

2 Organic Light-Emitting Diodes

This chapter provides a short introduction to the physical principles of organic semiconductors and their application in OLEDs.

2.1 Organic Semiconductors

The behavior of organic semiconductors is based on the properties of the carbon (C) atom. When atoms form bonds, their atomic orbitals are modified to molecular orbitals. The ground state of C is characterized through its electronic configuration as $(1s)^2(2s)^2(2p_x)(2p_y)$. In this ground state only two unpaired electrons can form bonds. The interaction with other atoms leads to a rearrangement of the orbitals. For C, hybrid orbitals are formed as linear combination of $2s$ and $2p$ orbitals. The mixing of orbitals minimizes the binding energy of the molecule through the optimal overlap of the atomic wave functions and is called hybridization [24].

The linear combination of orbitals leads to bonding and anti-bonding orbitals. Bonding orbitals can be interpreted as a constructive interference of the wave functions of the two involved electrons. Anti-bonding orbitals stand for a reduced electron density between the atoms. While bonding-orbitals have a lower energy than the orbitals for a single atom, the energy for anti-bonding orbitals is higher. In the ground state of the molecule all states until the highest occupied molecular orbital (HOMO) are occupied. The lowest energetic excitation is the transition of an electron from the HOMO to the lowest unoccupied molecular orbital (LUMO). The energy difference between HOMO and LUMO levels is often regarded as band gap, with an energy in the range of 2 eV to 5 eV. Compared to band gaps of inorganic semiconductors, for example silicon (Si) with 1.1 eV, this is relatively high. Due to the lower splitting of π-orbitals, the HOMO is a π-orbital, while the LUMO is an anti-binding π^*-orbital. Orbitals with rotational symmetry along molecular axes are called σ-bonds. They are strong, highly localized between the atoms and responsible for the strength of the bond. Orbitals above or below the molecular axis are π-orbitals. As the electron density is further away from the molecular axis, π-bonds are weaker than σ-bonds and delocalized. Because of this delocalization, the electrons in these bonds are responsible for the conductive properties in organic semiconductors [12].

Organic semiconductors can generally be divided into two classes: SM and polymer materials. SM are usually based on phenyl-rings and/or heteroatomic rings. In general, SM materials are vapor deposited, as their solubility is low in common organic solvents. Functional side chains can enhance the solubility of SMs, which enables solution processed devices based on SMs [20–22, 25]. Polymer materials consist of a long chain of repeating units, e.g., C atoms with alternating single and double bonds or aromatic rings, forming the polymers backbone. Their chemical behavior is determined by side chains [26–28].

The field of application of organic semiconductor materials includes, beside the aforementioned OLEDs, other electronic devices such as photovoltaic cells, thin-film transistors or sensors [29–31].

2.2 Organic Light-Emitting Diodes

The most simple device structure consists of an organic layer sandwiched between two electrodes. One electrode has to be transparent to allow light outcoupling. An applied voltage leads to the injection of holes from the anode into the HOMO and electrons from the cathode into the LUMO level of the organic semiconductor material. Under the influence of the electric field the charge carriers travel towards each other and form excitons. These strongly bound electron hole pairs can recombine under the emission of light. Such a simple device structure is not optimized for balanced charge carrier injection and transport. The most efficient OLEDs are multilayer devices, where each layer serves a specific task. For each task materials with appropriate properties are used. Charge carriers have to overcome an injection barrier at the electrode, which is determined by the difference between the work function of the respective electrode and the HOMO level for holes and the LUMO level for electrons. A hole injection layer (HIL) has a HOMO slightly lower than the work function of the anode. Transport layers balance the different charge carrier mobility values and shift the recombination zone towards the EML. The EML in general consists of a host molecule which is doped with an emitter molecule for light emission. The host molecule should have good transport properties for electrons and holes and generate excitons, which are then transferred to the dopant. A too high emitter concentration can lead to interactions between the emitter molecules which would negatively effect efficiency and color. The EML can additionally be surrounded by blocking layers, which prevent the respective charge carriers from leaving the EML without recombination. For an efficient OLED the materials have to be chosen to provide a gradient trough the energy levels. The emission color is mainly determined by the energy difference between HOMO and LUMO levels of the emitter molecule.

Charge transport in organic materials is more complex than in inorganic semiconductors, due to the localized states on the molecules and the small intermolecular interaction. After injection the charge carriers drift across the device following the local field. The strength of this field depends on the voltage applied, the device thickness and the distribution of space charges within the device [32].

A band like transport, where intermolecular interactions form delocalized energy bands in which the electrons and holes can move freely, only scattered by lattice vibrations, is typical for inorganic semiconductors. For some highly ordered organic crystals charge carrier transport can also be described with the band transport model. As organic semiconductors are characterized by a high degree of disorder and weak electronic coupling between molecules, charge carrier transport is depicted as hopping [27, 33], which describes the thermally activated tunneling of carriers between localized states. The charge carrier mobility can be construed as field and temperature dependent. Charge carrier mobility is generally lower in disordered organic semiconductors compared to organic crystals. Additionally the mobility of holes and electrons is different [34].

The charge carriers form excitons in the EML. As electrons and holes are fermions, their bound state has either $S = 0$ or $S = 1$. The combination of two particles with $s = \frac{1}{2}$ leads to four possibilities for the bound state. Excitons with spin $S = 0$ and spin quantum number $m_S = 0$ are called singlet excitons. As for $S = 1$, m_S has three possible values, these excitons are triplet excitons. The spins of the injected charge carriers are random, leading to a singlet to triplet ratio of $1:3$. The transition from the singlet to the ground state under light emission is called fluorescence. Singlet excitons have a lifetime of a few ns. The transitions of triplet states to the ground state is forbidden by spin selection rules ($\Delta S = 0$) and called phosphorence. Therefore, triplet excitons decay mainly non-radiative and their lifetime is much longer, up to

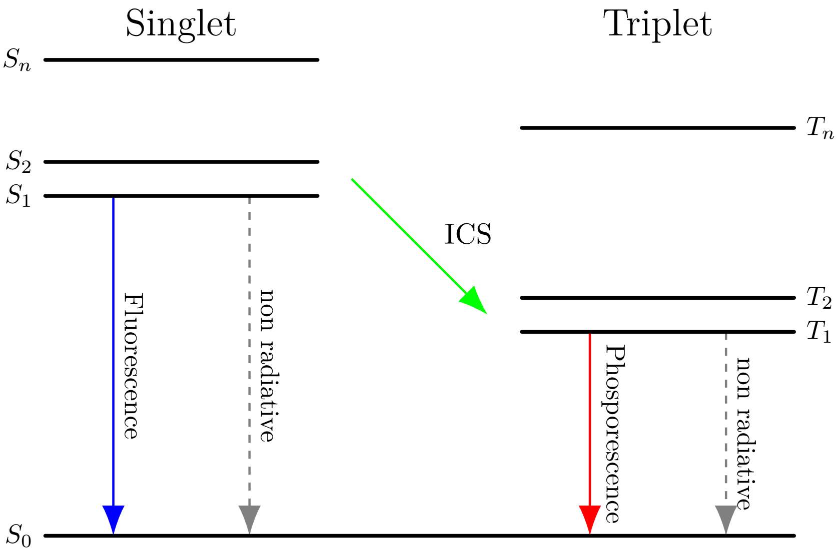

Figure 2.1: Basic Jablonski diagram representing the transitions between energy levels, such as fluorescence, phosphorescence, intersystem crossing and non-radiative decay.

some ms. The Jablonsky diagram in figure 2.1 shows the transitions between energy levels schematically. For fluorescent emitters only 25 % of the injected charge carriers contribute to light emission. There are several approaches to also harvest triplet states [35]. One example is the use of molecules with transition metals such as iridium (Ir), platinum (Pt) or ruthenium (Ru) [36]. The transition metals induce strong spin-orbit coupling, which results in mixing of singlet and triplet states [12]. Triplet emitters have to be embedded in a suitable host matrix, as the long triplet lifetime otherwise leads to triplet-triplet annihilation. In conjugated polymers a higher singlet generation can be found [37].

OLEDs are often categorized through the deposition technique of the materials used. A well established method is vapor deposition [35]. It is mainly used for SM materials. Materials used have to be thermally stable. In a simple variant, the materials are placed in heated crucibles in a high vacuum deposition chamber and evaporated. The substrate is placed above the crucibles. Shadow masks can be used in between to structure the layers. The deposition of several different layers on top of each other, which is necessary for complex multilayer structures, is easily achievable with this technique. The flux of the sublimed material and the temperature of the substrate can be aligned to control the growth of the material. Therefore a high accuracy over a wide range of thickness values is achievable. The evaporation also increases the purity of the material. The disadvantages of the technique are the high complexity and the high material consumption. Also the production of patterned structures in large scales is limited by the handling and the accurate positioning of the shadow masks [6].

Solution processing promises an easy and cost efficient deposition of organic layers in large scales. Usually this method is used for polymers, but solution processable small molecules do exist [25]. Typically organic solvents such as toluene or chloroform are used. In lab scales spin coating is mainly preferred. A drop of the solution is placed on the rotating substrate. The solution is spread into a film that covers the substrate with a uniform thickness. The solvent evaporates while spinning, but most films are annealed afterwards to get rid of solvent residues. The annealing steps normally include heating the layer for a certain time. As the annealing process represents an additional energy supply to the system, it can lead to changes in the material. The concentration of the material in the solution, the spinning speed and the viscosity determine the film thickness [32]. The controlled fabrication of multilayer structures, which are required for efficient OLEDs, is more difficult to achieve with solution processing [38]. The solvents used for one layer can partly dissolve the previous layer, which can lead to unwanted intermixing. Different strategies to avoid these challenges exist. A simple approach is to use different solvents [39]. Another one is to reduce the solubility of the polymer film after deposition by annealing or exposure to ultraviolet light [18].

The efficiency of OLEDs is determined by a number of physical processes, such as the injection and transport of the charge carriers and their recombination. The ratio between the number of emitted photons and injected charge carriers is the external quantum efficiency (EQE), which is a function of the internal quantum efficiency (IQE) factor η_{IQE} and the outcoupling factor η_{OUT} [2].

$$\eta_{EQE} = \eta_{IQE} \cdot \eta_{OUT} = \gamma \cdot \eta_{S/T} \cdot \phi_{PL} \cdot \eta_{OUT} \tag{2.1}$$

The IQE describes the ratio of photons produced in the device to injected charge carriers and depends on the charge carrier balance γ, the ratio of singlet to triplet excitons $\eta_{S/T}$ and the photoluminescence quantum yield ϕ_{PL}. The charge carrier balance γ is determined by the probability that holes and electrons recombine and form excitons. It can be maximized by balancing the numbers of electrons and holes.

The photoluminescence quantum yield describes the portion of excitons, which decay under light emission. All non-radiative decays, such as vibronic relaxation or internal conversion, reduce ϕ_{PL}.

As mentioned before the ratio of singlet to triplet excitons is in general 1:3. For fluorescent emitters the factor drops to $\eta_{S/T} = 0.25$, while it reaches $\eta_{S/T} = 1$ for phosphorescent emitters.

The IQE can reach nearly the theoretical limit of 100 % in an optimized device set up, which means that almost all injected charge carriers recombine and all excitons decay radiatively. After all only a fraction of the emitted photons can escape the device, which is described by the outcoupling factor η_{OUT}. In a planar device η_{OUT} can be estimated by [40]:

$$\eta_{OUT} \approx \frac{1}{2n^2} \tag{2.2}$$

The factor n is the refractive index of the organic material. For typical values of n only about 20 % of the generated photons are able to escape the device [41].

From the equations describing the efficiency it is easy to see which parameters have to be optimized: amongst others balancing the number of injected charge carriers, reducing injection barriers and adjusting for the different mobilities of holes and electrons. A reduction of trap states minimizes charge carrier losses, for example through the use of purified materials. The use of phosphorescent emitters enhances exciton harvesting. For multilayer devices it is crucial that no intermixing of layers happens while or after deposition, as the function of the individual layers can be disturbed by molecules of other layers.

Other challenges are the encapsulation of the organic material and different degradation rates depending on the emission color. The lifetime of blue pixels is significantly lower than for red pixels, which leads to a color shift towards the red spectrum in aging displays [2]. OLED materials are typically sensitive to oxygen and water and therefore need a barrier to protect them from environmental influences [7, 11].

3 Methods

The following chapter gives a short introduction to analytical methods, used for sample characterization.

3.1 Electron Microscopy

Electron microscopes use a high energy electron beam to create an image of the sample. Due to the wave-particle dualism the kinetic energy of the electrons determines their wavelength [24]. At energy values typically used in electron microscopes the wavelength of electrons is much smaller than the wavelength of photons used in light microscopes. With electrons it is possible to achieve higher magnification than those set by the magnification limit in visible light microscopes. In the following chapter a short introduction to the physical principles of the interactions of electrons with matter is given. These interactions are the foundation to functionality and properties of electron microscopes.

3.1.1 Interaction of Electrons with Matter

Complex interactions between high energy electrons and sample atoms lead to a multitude of different signals. Electron microscopy can therefore provide information on sample structure, topology, morphology and composition. As electrons are low-mass, negatively charged particles, they are easily deflected when passing the positive nucleus of atoms or other electrons in the shells. In general the interactions are classified into two groups, namely inelastic and elastic scattering.

Electrons can interact with the sample's atoms elastically, which means its trajectory changes but its kinetic energy is almost unaltered. Inelastic interactions lead to an energy transfer from the electron to the sample. This energy transfer gives rise to different signals, such as Auger electrons, secondary electrons (SEs), X-ray photons, plasmons, phonons or cathodoluminescence. These signals can be used to attain further information about the sample. On the other hand, the energy transfer can also lead to sample damage.

- Inner-shell ionization

  A high energy beam electron can transfer enough energy to an inner shell electron, so that it is able to escape the shell and leaves behind an electron vacancy called a hole. The ionized atom returns to its ground state by filling the hole with an electron from an outer shell and emitting the excess energy. These energy can either be emitted as a characteristic X-ray photon or an Auger electron. In both cases the emitted energy is determined by the energy difference of the involved shells and characteristic for the particular atom. Analysis of this energy can be used to determine the sample composition. For higher shells involved also non radiative Coster-Kronig transitions are possible, which are rearrangements within subshells.

- Bremsstrahlung

  Bremsstrahlung is emitted when an electron is slowed down by the Coulomb field of the nucleus. The energy of these X-ray photons can be up to the beam energy. In general a smaller energy loss is more likely. Bremsstrahlung shows a strong forward scattering and its intensity increases with the average atomic number (Z) of the specimen. Usually Bremsstrahlung leads to an unwanted spectral background when analyzing characteristic X-rays emitted from the sample.

- Secondary electrons

  SEs are weakly bound electrons from outer shells, that are ejected by the incident electron beam. The energy transferred is relatively low, leading to small kinetic energies of the SEs. They are generated within the whole interaction volume, but due to their low energy only those created in surface near regions are able to escape the sample surface. SEs have an energy below 50 eV, with a most probable energy of about 2 eV to 5 eV.

- Phonons

  An incident electron can transfer energy to an atom directly. This atom begins to vibrate and influences neighboring atoms, which leads to a distribution of the transferred energy over a large volume. The collective vibrations correspond to sample heating, which can lead to sample damage. Cooling the sample reduces this effect.

- Plasmons
  If the incident electron passes through free-electron gas, it can induce collective osscillations of the electron gas. Plasmons can occur in all materials with free or weakly bound electrons.

- Cathodoluminescence
  The inelastic scattering of high energy electrons can lead to the emission of low energy photons with an energy range of 1 eV to 5 eV, which corresponds to infrared, visible and ultraviolet light. Cathodoluminescence occurs in insulators or semiconductors, with a filled valence band and a separated conductive band. The impinging electron transfers energy to a valence electron and transfers it to the conduction band, leaving behind a hole. The excited state can relax by an electron dropping from the conduction band. The excess energy is emitted as a photon carrying the energy difference.

The depth an electron can reach before its kinetic energy has vanished due to multiple inelastic scattering events is called penetration depth. As the scattering processes broaden the incident beam, a pear shaped volume is formed beneath the sample surface. The penetration depth rises with increasing energy of the incident beam and falls with rising Z [42,43].

3.1.2 Scanning Electron Microscopy

Modern scanning electron microscopes (SEMs) are versatile instruments for surface analysis and have a wide variety of applications in materials science, semiconductor industry and life sciences. Sample requirements are moderate and the image interpretation is relatively simple.

The main components of a SEM are an electron column with the electron gun, magnetic lenses and coils, a sample chamber with a movable sample stage and a detector system. The high vacuum environment in the instrument with a pressure lower than 10^{-4} Pa minimizes the interaction of electrons with residual gas molecules. In the electron gun electrons are emitted from a cathode and accelerated towards a ring-shaped anode by the voltage difference between the two electrodes, which is adjustable and typically in the range of 0.5 kV to 30 kV. The beam is focused on the sample surface through at least two electromagnetic lenses within the electron column. A typical size of the electron probe is 10 nm. At this size the electron beam has still enough probe current to allow for a reasonable signal to noise ratio. The probe size determines the achievable resolution. The electron probe is scanned across the sample surface in two perpendicular directions by pairs of beam deflecting coils. The dwell time is the time the electron beam stays at one certain pixel. Short dwell time values are used for live imaging of the sample for focusing or the search for certain features. Dwell time values up to ms are used for images with higher quality. The image produced by the detector is a two dimensional intensity map. Detectors are either mounted at the side of the electron column above the sample or in the lens above the objective lens within the electron column [44].

The impinging electrons interact with the atoms of the sample material, leading to elastic and inelastic scattering of the electrons with a number of different signals as described in section 3.1.1. In a SEM the most used interaction products for imaging are SEs and backscattered electrons (BSEs). As SE have a relatively low kinetic energy, only the fraction created very near to the surface can escape the sample and reaches the detector. Therefore the signal, which can be derived from the detection of SEs, provides information about the properties of the sample surface. Surface features facing the detector appear brighter, as the electrons generated in these regions have a higher probability to reach the detector. SE images have therefore a three-dimensional appearance [45].

Most of the elastic scattering of electrons in the specimen happens with a scattering angle of less than 90°. Only a small fraction of electrons are backscattered with a deflection angle $\theta > 90°$. Due to their high kinetic energy, slightly below the primary beam energy, these BSEs can exit the sample and be detected. The deflection of a BSE can be caused by a single scattering event or an accumulation of several scattering events with an angle lower than 90°. BSE images show contrast regarding different sample composition, as the number of primary electrons, which manage to escape the sample as BSE increases with the atomic number. Due to their higher energy the depth from which BSE can escape is higher than for SE.

One advantage of the SEM is the high depth of focus, which means sample features with a high range of distances to the source are in focus. Another advantage is the possibility to measure bulk samples and a wide range of applications. The sample requirements are that it is stable in the high vacuum environment and has a sufficient electrical conductivity. Low conductivity can lead to local charges which disturb particularly the SE emission, due to their low energy. Positively biased surfaces hinder SEs at their escape from the sample surface and appear darker. Negatively charged surfaces repel the SEs and therefore appear brighter in the image. Non conductive samples can be coated with a thin film of conductive material such as gold (Au) or C. A lower acceleration voltage also facilitates the analysis of samples with low conductivity.

3.1.3 Transmission Electron Microscopy

Transmission electron microscopes (TEMs) are used to investigate structure and composition of thin samples on a submicron scale. TEMs have a wide variety of applications in fields like material science, chemistry or biology.

The beam path in a TEM is similar to a light microscope. The electrons are emitted by an electron gun, accelerated and focused onto the specimen by a condenser lens. The electrons interact with the sample atoms and the transmitted beam is focused by the objective lens to form an image. This image can be viewed by a fluorescent screen or recorded by a charge-coupled device (CCD) camera. An objective aperture is used to enhance image contrast [46]. When the objective lens is adjusted to only allow the central beam and forward scattered electrons with small deflection angles to pass, a bright field (BF) image is formed. For a dark field image electrons with higher scattering angles are used.

The contrast in TEM images is mainly determined by elastically scattered electrons. For amorphous samples the most important contrast mechanism is the so called mass-thickness contrast. It is formed by the two following principles. As stated before, the probability that an electron is deflected by the Coulomb field of an atom is dependent on the number of charges in the atom, described by Z. As light elements scatter less than heavier atoms, sample regions with a low mean Z appear bright, while those with heavier elements appear dark. In addition, the probability of a scattering event increases with sample thickness and therefore thick areas of the specimen appear dark [45]. In dark field images the contrast is reversed.

In crystalline samples the regular arrangement of atoms leads to coherent elastic scattering. The interference of the scattered electrons forms a diffraction pattern. The Bragg equation describes the relation between the interatomic distances and the diffraction angle. While for single crystal samples the diffracted electrons form spot patterns, polycrystalline materials lead to ring patterns, which are superimposed spot patterns. The spots or rings can be assigned to a certain plane or planes of the crystal lattice.

A major limitation of the TEM is the need for thin specimens as they have to be electron transparent. As a general rule a TEM specimen should have a thickness of less than 100 nm. However, which exact thickness appears electron transparent is dependent on the electron energy and the averge atomic number in the sample [43].

In a conventional TEM set up a defined sample area is illuminated. In a scanning transmission electron microscope (STEM) a small electron probe is scanned in a raster across the sample. As each point of the sample surface is irradiated independently, EDX and electron energy loss spectroscopy (EELS) are conducted in STEM mode. While dedicated STEMs are available, conventional TEMs are often equipped with additional deflection coils and detectors for STEM mode.

3.2 Focused Ion Beam

The FIB technology is a versatile tool for the fabrication of microstructures and used in fields like material science or semiconductor industry. The functionality of FIB includes imaging, milling and deposition. With the combination of milling and deposition the creation of complex three-dimensional structures with high precision and reproducibility is possible. An important application is the preparation of thin samples for TEM, so called lamellas [47, 48].

The basic set up of a FIB instrument is similar to a SEM. While stand alone FIB instruments are available, FIB columns are often integrated in other analytical instruments, mainly SEMs. The main components are the ion column with a liquid metal source, a movable sample stage, detectors and the vacuum system. The ion source consists of a tungsten (W) needle which is attached to a reservoir with liquid metal. The most common source material is gallium (Ga), due to its low melting point. Heated Ga wets the W tip and an electric field forces Ga ions to leave the tip. The extracted Ga ions are accelerated through an electrical potential down the column with voltage values ranging from 5 keV to 50 keV. The ion beam is focused through electromagnetic lenses. Apertures define the probe size and provide different ion currents from few pA to 30 nA. Deflecting lenses allow for scanning the beam across the sample surface.

The ion beam can be used to image the sample surface, to mill or to deposit material. Milling is the consequence of physical sputtering, which occurs as the result of a series of elastic collisions. Momentum is transferred from the incident ions to the sample atoms. An atom of the surface can receive enough kinetic energy to overcome the surface binding energy. The emitted atoms can also be ionized and may be detected for imaging or mass analysis. Results of inelastic scattering events are phonons, plasmons in metals and SEs. The latter are used for imaging. For non conducting samples also secondary ions can be used for imaging. The charge accumulation due to the incident Ga ions can lead to a local positive charge, which inhibits SEs from escaping the sample surface. These areas will appear dark in an SE image, but an secondary ion image will not be effected. As the interactions between the ions and the sample reduce the ions kinetic energy, ions that are not backscattered out of the sample will be implanted at some depth below the sample surface. Imaging in a FIB system always leads sample damage, due to implantation and milling. The use of low ion currents reduce especially the latter effect.

Ion beam assisted chemical vapor deposition can be used to deposit metals like Pt, Au and W from organometallic precursor gases. The deposition of insulating materials such as silicon dioxide (SiO_2) is also possible. The capillary of the gas injection system (GIS) is positioned above the sample surface close to the preferred deposition site. The precursor gas molecules exit the nozzle and are adsorbed at the surface. The decomposition of the precursor gas only occurs on ion impact. Repeated adsorption and decomposition leads to a build up of material in the scanned region. Therefore the process is a fine balance between sputtering and decomposition. The deposited material includes beside the desired metals also incompletely decomposed precursor molecules and Ga implants. The particular composition is dependent on the deposition conditions.

3.3 Dual Beam Instruments

The combination of a SEM with a FIB offers advantages for sample preparation. While the FIB can be used to structure the specimen by milling or depositon, the electron beam images the sample non-destructively. The typical configuration in a dual beam instrument consists of a vertical electron column and tilted ion column, as the ion column is usually more compact. The columns are aligned to have a coincident point, where both beams image the same spot of the sample. The inspection of the side wall of a structure, cut with the ion beam, would require tilting the sample in a FIB only instrument and also the change to a lower ion beam current. Furthermore, the inspection with the electron beam prevents additional ion implants.

For delicate samples it is also possible to deposit a thin material film with the electron beam, before adding the rest with the ion beam. This decreases the implantation of Ga ions into the sample, when the layer of interest is directly underneath the sample surface.

Another application of dual beam instruments is the so called slice and view technique. It can be used to investigate the three dimensional structure of the sample. After milling a certain amount of the sample material, an image with the electron beam is recorded. Milling and imaging are repeated. The consecutive image sequence can be used to reconstruct the three dimensional structure of the sample. The alternating milling and imaging process can also be automated [47].

3.4 Energy Dispersive X-ray Analysis

As stated in section 3.1.1 the inelastic scattering of electrons in the sample can lead to inner shell ionization and the emission of characteristic X-ray photons. The detection and analysis of this photons allows the identification of the chemical composition. The photons can either be analyzed using a wavelength dispersive detector system consisting of a goniometer, crystal and detector or in an energy dispersive detector. Despite having a lower energy resolution and an increased background, EDX is more commonly used than wavelength dispersive X-ray spectroscopy (WDX) in electron microscopes. The advantages of EDX are the compact design and the shorter acquisition time due to simultaneous multielement spectrum acquisition. Both SEMs and TEMs can be equipped with X-ray detectors. In general the X-ray intensity is higher in SEMs because of the bulk sample. The spatial resolution of EDX is limited, as the X-ray photons are generated in the whole excitation volume.

The characteristic photons are identified by a combination of the shell, in which the hole was located, and the shell from which the electron originates, which filled the hole. A photon which is emitted after a hole in the K shell is filled by an electron from the L_{III} shell is termed $K\alpha_1$. The according line when an electron from the M_{III}

fills the hole is $K\beta_1$. Further lines and their naming scheme are shown in figure 3.1. The energy of a characteristic X-ray photon is determined by the energy difference between the involved energy levels.

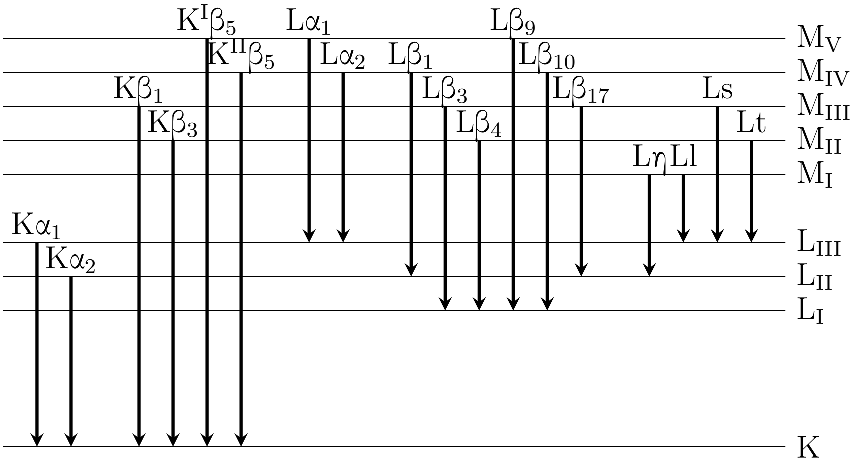

Figure 3.1: X-ray emission lines corresponding to transitions between K-, L- and M-shell and their naming scheme after Siegbahn, adapted from [49].

Energy resolved detection of X-rays is based on their interaction with a suitable detector material, nowadays usually a semiconductor. State of the art EDX detectors are silicon drift detectors (SDDs), with the ability to process high count rates and the advantage of simple, integrated peltier cooling. When an X-ray photon enters the active volume of the detector, electron hole pairs are generated. The number of charge carrier pairs is directly proportional to the energy of the incident photon. This signal is amplified and analyzed using a multichannel analyzer, which sorts and stores the pulses to the according energy channel [45, 50]. For SDDs the typical maximum energy is set to 10 keV or 20 keV with 2048 channels, which corresponds to 5 eV or 10 eV per channel. In principle the SDD is also able to measure higher energy X-ray photons, but due to the decreasing probability of interaction with increasing energy and the low thickness of the active area of the detector (some 100 µm), high energy photons are able to transmit through the detector without being completely absorbed.

3.5 Grazing Incidence X-ray Fluorescence and X-ray Reflectometry

X-ray fluorescence (XRF) is the emission of characteristic X-ray photons from a material irradiated with an X-ray beam. In conventional XRF, X-ray source and detector enclose an angle of 45° to the sample and 90° between each other. A variant of this technique is total reflection X-ray fluorescence (TXRF). Here the incident X-ray beam impinges on the sample surface at a very small angle so that the beam is totally reflected. The detector is placed directly above the sample at a very small distance to the surface. The advantages of TXRF are an improved signal to background ratio, the double excitation from incident and reflected beam and the large solid angle due to detector placement. All this combined leads to very low detection limits in the femtogram region for a fast, multielement analysis [51].

Contrary to visible light the refractive index in the X-ray regime for a given material is a complex number and can be written as [52]

$$n = 1 - \delta - i\beta \tag{3.1}$$

with the real term δ, which is associated with dispersion, and an imaginary part β, which describes the absorption. For most materials the real part of the refractive index in the energy region of X-rays is slightly smaller than unity, which leads to a total external reflection at an interface air or vacuum to material [53]. The critical angle, below which total reflection of X-rays can be observed is dependent on the real term δ. Below the critical angle, incident and reflected beams interfere and form an X-ray standing wave (XSW) on the sample surface and the penetration depth of the X-rays is only a few nm. With increasing incidence angle the positions of the XSW modes shift into the sample material. The penetration depth is increased rapidly and the intensity of the fluorescence signal changes [54]. These changes due to a variation of the incidence angle are used to characterize the samples with grazing incidence X-ray fluorescence (GIXRF) and X-ray reflectometry (XRR).

For GIXRF the fluorescence signal is measured as a function of the incidence angle of the primary X-ray beam. The incidence angle is varied across the critical angle for total reflection. With increasing incidence angle the penetration depth of the primary X-rays becomes larger, which provides information of the elements in sample and substrate material. As the XSW is determined by the interference of the signals from different layers, the fluorescence signal provides information on the layer sequence and the depth distribution of the elements present [55]. Additionally, layer thickness, density and roughness of the films can be determined [52]. GIXRF is used for depth profiling and characterization of thin layers in depths of up to a few hundred nm.

For XRR, the specular reflection of the primary X-ray beam is measured, while varying the incidence angle. The reflectivity depends on the electron density of the material and its variation with depth. At the critical angle the reflectivity signal drops sharply. The signals of thin layers again lead to interference, which leads to fringes in the reflectivity curve. The spacing of the fringes correlates with layer thickness. The general form of the curve is related to the layer roughness [55]. XRR can determine thickness and roughness of thin films with a thickness range from few to hundred nm [56].

Both methods are based on the comparison of measured and calculated data [57]. For the calculations, the samples are modeled based on parameters such as layer sequence, their composition and thickness, surface/interface roughness and density. Instrument parameters like X-ray beam divergence or the inspected area also need to be taken into account. Unfortunately, the results of these calculations can be ambiguous for both methods on their own, as different sample models can lead to similarly good results. Using a combination of GIXRF and XRR is beneficial, as it reduces uncertainties of the individual method [52, 53, 58].

Combined GIXRF/XRR measurements can be performed with dedicated spectrometers or an X-ray diffractometer with an additional fluorescence detector [59, 60].

3.6 X-ray Photoelectron Spectroscopy

X-ray photoelectron spectroscopy (XPS) is a surface sensitive, nondestructive method to determine and quantify chemical composition and speciation of elements for a wide variety of samples. All elements from lithium to uranium are detectable. The sample is irradiated with an X-ray beam, photons interact with core electrons and when their energy is sufficient electrons can leave the shell. The kinetic energy E_{kin} of these so called photoelectrons is measured in an electron detector and is given by

$$E_{kin} = h\nu - E_{bin} - E_W \tag{3.2}$$

where $h\nu$ stands for the photon energy, E_{bin} describes the electron binding energy and E_W accounts for the work function of the instrument [61]. The energy distribution of the photoelectrons give a spectrum with a series of peaks. The presence of peaks at characteristic energy values allows the identification of elements. The binding energy is also altered by the chemical environment of the atom, which facilitates the identification of the element's chemical bond. The peak area can be used to determine the element's concentration [62]. The surface sensitivity of the technique is due to the depth from which the photoelectrons are able to escape and is smaller than 10 nm for most materials.

An XPS spectrometer consists of an X-ray source, an appropiate sample holder, an electron analyzer and an electron detector. As X-ray source serve mainly X-ray tubes with aluminum (Al) or magnesium (Mg) or dual Al/Mg anode. Measurements have to be performed under high vacuum conditions to reduce the disturbance of the emitted photoelectrons through residual gas and to minimize sample contamination. The system which analyzes the electron energy consists of three parts. The collection lens in modern systems has a solid angle larger than 20°, which improves the number of photoelectrons collected. The electrostatic fields of a concentric hemispherical analyzer only allow electrons with a given energy to reach the detector. This energy is called pass energy. Typically 5 eV to 25 eV pass energy values are used for high resolution spectra for particular elements, while higher pass energy values at 200 eV are used for survey scans [63].

Non conductive samples need an additional source of electrons to prevent a positive charge built up through the loss of photoelectrons. A so called flood gun provides low energy electrons to establish an equilibrium in the sample.

Although XPS is a highly surface sensitive method, these first few nm of a sample can have a different composition. A method to evaluate the composition as function of the depth is to tilt the sample while X-ray tube and detector remain fixed. This extends the path for electrons in deeper layers and therefore favors particular signals from surface near regions with increasing sample angle [63].

4 Experimental

This chapter presents the sample preparation and characterization using the methods introduced above. Measurement procedures and conditions as well as evaluation and interpretation of the collected data are described.

4.1 Samples

All samples characterized in this thesis were manufactured by Merck KgaA.

Samples for TEM investigations were fabricated on square glass substrates, partly coated with a 50 nm thick indium tin oxide (ITO) layer, which forms the transparent anode. The organic layers were either spin coated or vapor deposited onto the substrate. Lastly, on top of the organic layers, Al contacts were vapor deposited using a shadow mask. The number and sequence of the layers as well as the materials used are dependent on the respective question. Therefore the exact sample composition is specified at the beginning of the particular results chapter. The complete layer sequence is present in the overlapping part of the two contacts forming a so called pixel.

All samples were stored under nitrogen atmosphere in a glove box to prevent degradation by oxygen and water, as they were not encapsulated. To investigate a pixel the substrates were broken into single pixels. The pixels were mounted on a SEM sample holder for sample preparation by FIB milling. Contacts were connected to the sample holder using conductive silver paint.

Samples for GIXRF/XRR analysis were fabricated on quartz substrates. The use of substrates with ITO contacts, which do not cover the whole substrate, would lead to unwanted edge artifacts, which can not be modeled in the software used for data analysis.

4.2 Lamella Preparation

This chapter summarizes the necessary steps to obtain electron transparent lamellas of the cross section of organic layer stacks.

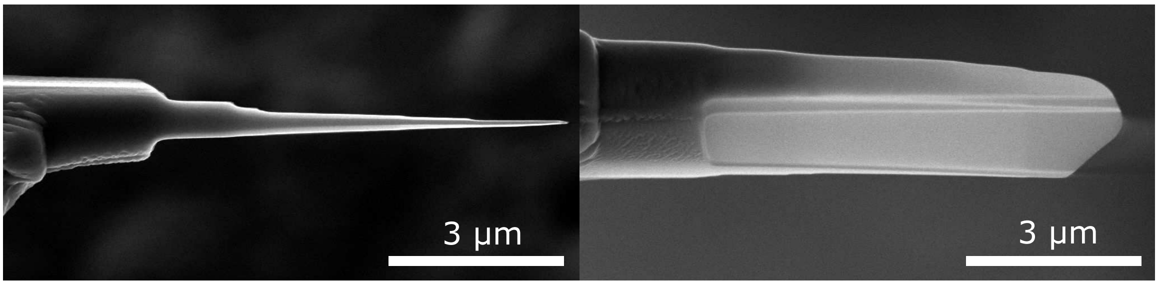

Figure 4.1: SEM image of a wedge shaped TEM lamella (left: top view, right: side view at an angle of 52°).

For TEM analysis thin, electron transparent samples are required. An electron transparent lamella should have a thickness of less than 100 nm, in order to obtain high quality images [45]. In general, TEM lamellas are manufactured with a uniform thickness. For STEM-EDX measurements, the low thickness combined with the organic material may lead to insufficient characteristic X-ray emission for the elements of interest, and, therefore, to unsatisfactory statistical quality of the X-ray data acquired. Increasing the spectrum acquisition time is one possible solution to obtain a higher intensity signal. However, due to damage of the sample material by the 200 keV electron beam [64], the measurement time cannot be increased indefinitely. Another way to increase the EDX signal is to measure thicker samples, as this increases the total interaction between electron beam and sample material. However, increasing thickness reduces electron transmission, leading to decreasing image quality.

To obtain samples which are electron transparent, on one hand, but also yield reliable EDX data, on the other, lamellas were deliberately thinned into a wedge shape [65]. A wedge shaped lamella is shown in figure 4.1. Near the tip high quality TEM images can be recorded. In the middle of the thinned part of the lamella, at a thickness of about 200 nm to 300 nm, EDX measurements can be performed, with sufficiently low beam damage while obtaining a good EDX signal. A major drawback when analyzing a thicker part of the lamella is a decreased spatial resolution, due to enlarged interaction volume. However, this has only little effect on the measurements in this thesis, as the particular organic layers are relatively thick. Thus, preparing wedge-shape lamellas was an ideal sample preparation method to obtain high quality TEM images as well as good EDX spectra from the same sample. Additionally, the wedge shaped form provided a higher long term stability of the lamellas, which facilitated repeated measurements.

4.2.1 Focused Ion Beam Milling

To obtain a thin specimen of the cross section of the layer stack for TEM investigation a TEM lamella has to be cut. For analysis the slice has to be transferred to a TEM lift out grid and thinned to reach electron transparency.

For FIB milling, it is necessary to tilt the sample to be perpendicular to the ion beam. In the helios dual beam instrument the required angle of the sample stage is 52°. After identification of the overlapping region of ITO and Al contacts, a Pt protection layer is applied to the sample surface in the area of interest (see figure 4.2a). The Pt layer protects this sample area from the Ga ion beam during further preparation. The process of Pt deposition is described in section 3.2.

The Pt precursor used in the Fei helios nanolab is Methylcyclopentadienyl platinum trimethyl $(CH_3)_3(CH_3C_5H_4)Pt$. For a less damaging deposition, a thin layer of Pt can be deposited using the electron beam.

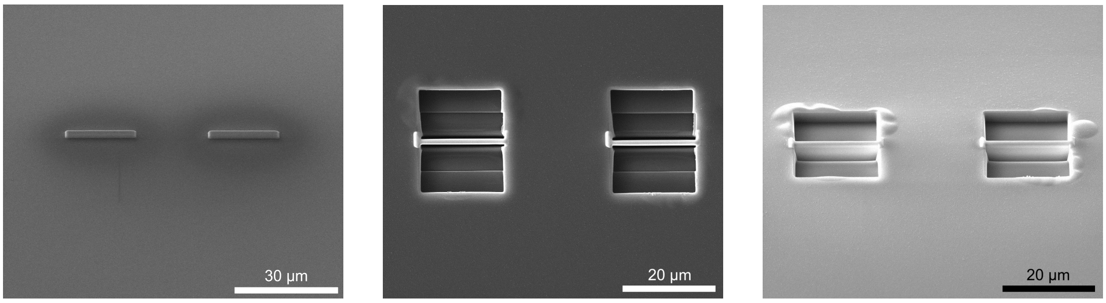

(a) (b) (c)

Figure 4.2: SEM-images of lamella preparation: (a) deposited Pt protection layer, (b) lamellas after RCS, (c) lamellas after CCS.

In the next step the lamella is excavated. The ion beam is used to remove sample material on two sides of the Pt layer. Removal is done by cutting defined patterns in the sample surface. The two patterns used are "Rectangle" (figure 4.2b) and "Regular Cross Section". The first creates a uniform deep rectangle shaped hole into the sample. The latter provides a stair step shape. For patterns with the same base area dimensions, with regular cross section (RCS) less material has to be milled, leading to a shorter completion time and reduced material redeposition.

The lamella is polished using cleaning cross sections (CCSs) with decreasing ion beam current, to remove unwanted redeposited material (figure 4.2c). When the lamella has been cut to a thickness of about 1.5 µm, it is ready for the next step.

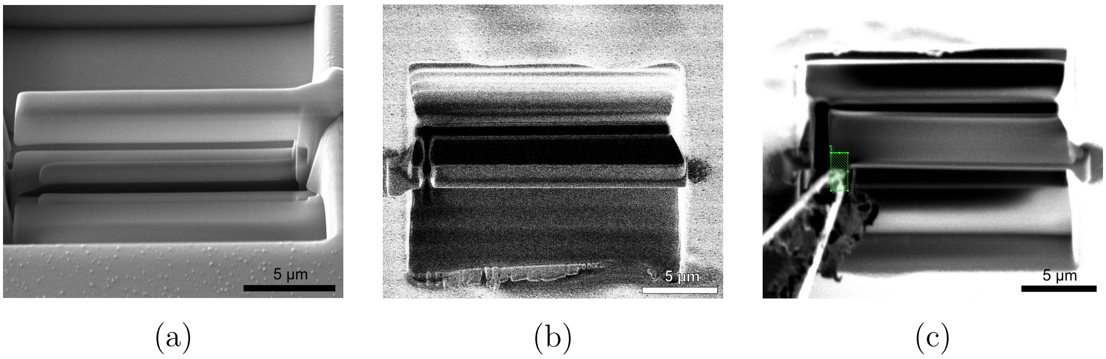

(a) (b) (c)

Figure 4.3: SEM image of lamella (a) L-cut, FIB images: (b) lamella before approach of MM, (c) lamella with MM tip and rectangle pattern for Pt deposition.

To transfer the lamella to a TEM grid a micromanipulator (MM) with a W needle tip is used. The lamella is detached from the bulk of the sample at the bottom and the left side (figure 4.3a and b). First the bottom is cut free using a slim rectangle pattern and a high ion beam current. Then the left side is detached using a CCS pattern. Which pattern works best for which step and the sequence of the cuts has been determined by variation and evaluation of outcomes. The goal is to reduce material redepositon which leads to reattachment of the lamella to the bulk sample. For the undercut it can be helpful to tilt the sample to increase the angle of the ion beam relative to the sample. This was not necessary for the 1.5 µm thick lamellas.

The MM tip is cautiously moved towards the sample surface. Before it is close to the lamella, the GIS needle for Pt deposition has to be inserted, to avoid damage to the lamella if the GIS needle hits the micromanipulator tip. The tip is moved to contact the left side of the lamella and attached to it using Pt deposition, as can be seen in figure 4.3c. The lamella is then completely detached from the sample bulk by cutting the right side using a CCS pattern (figure 4.4a). When the lamalla is free from the bulk, it can be lifted carefully using the micromanipulator controls (figure 4.4b).

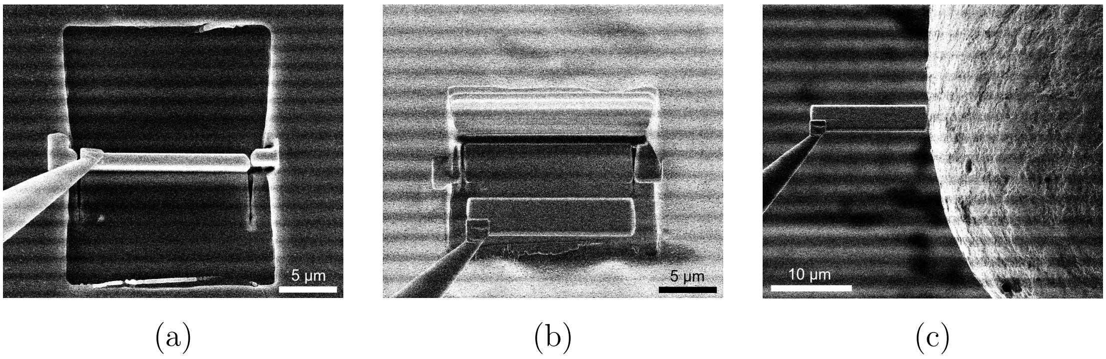

(a) (b) (c)

Figure 4.4: SEM image of lamella (a) after final cut, FIB images: (b) lamella after the careful lift out, (c) lamella after careful approach towards the TEM grid.

After successful removal of a TEM lamella from the sample it needs to be attached to a TEM sample holder, a so called TEM grid. The lamella has to be carefully moved towards the TEM grid (figure 4.4c). This is the most crucial step as slips from the piezo motors of the MM or a quick approach can lead to a collision between the lamella and the grid. A collision usually results in loss of the lamella, as the connection by the deposited Pt between lamella and tip is not very strong. Again the GIS needle should be inserted before the lamella is too close to the grid.

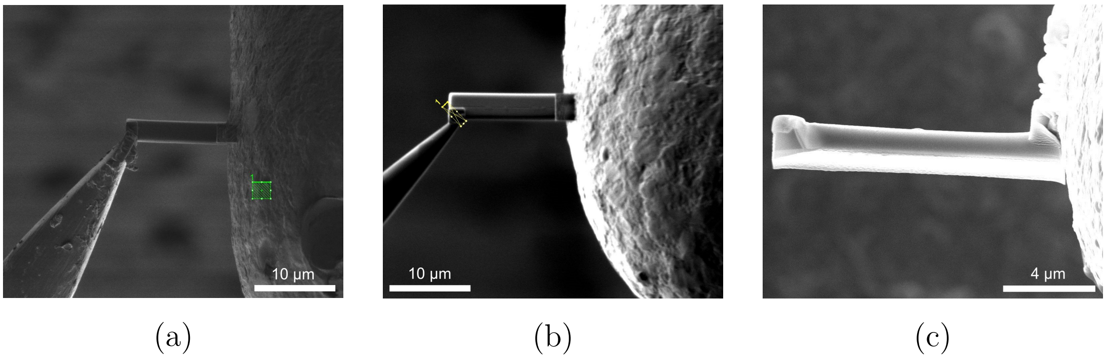

(a) (b) (c)

Figure 4.5: FIB images: (a) after Pt deposition to attach the lamella to the grid, (b) pattern to cut lamella free from MM tip, (c) SEM image of lamella on the TEM grid.

When the distance between lamella and grid is smaller than a few nm it is attached to the grid with Pt deposition (figure 4.5a). The lamella then is cut from the tip (figure 4.5b). This cutting should happen shortly after the attachment. The MM needle tip should be cleaned before it is used again, as there is still Pt left on it. This is done by placing the tip on an unused side of the sample area, e.g. areas with conductive silver paint. Then the ion beam can be used to remove Pt residue.

The transferred lamella is not yet suitable for TEM investigation as its thickness is still too high. In the following steps the lamella has to be thinned. This is accomplished by careful FIB milling. The correct lamella position is determined with the electron beam first to reduce sample damage. First thinning steps are carried out at an angle of 2° above or beneath the angle at which the lamella appears vertically in the respective image. This undercuts the glass substrate at the bottom of the lamella in order to reduce redeposition of glass material at later thinning steps. Starting with the ion beam current of the last pre thinning step (for example with 0.43 nA) thin CCS are positioned at the lamella's edge (figure 4.6a).

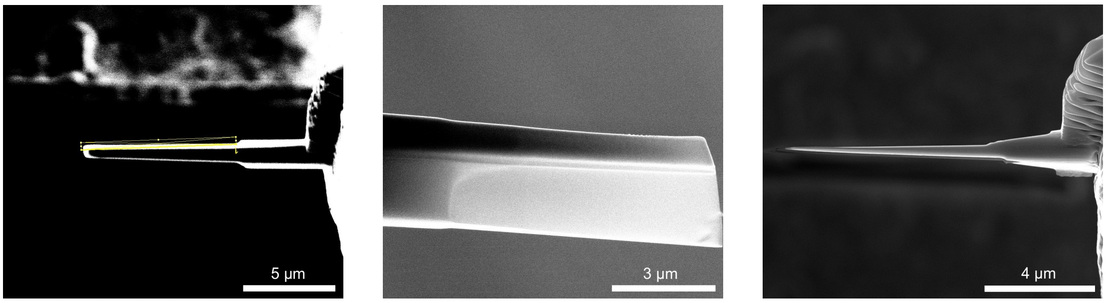

(a) (b) (c)

Figure 4.6: FIB image: (a) rotated CCS pattern while thinning, SEM images: (b) electron transparent lamella after thinning, (c) thinned, wedge shaped lamella.

The electron beam can be used to monitor the milling progress. The thinner the lamella, the more carefully the patterns have to be placed. The last thinning steps should be performed with lower acceleration voltage for the ion beam, e.g., 16 keV instead of 30 keV. Unfortunately not all samples can be focused well enough with this setting. The thickness of the lamella should be checked regularly in the electron beam image (figure 4.6a).

In general, TEM lamellas are manufactured with a uniform thickness. The lamellas for this work have been thinned into a wedge shape. This is accomplished by rotating the patterns relative to the lamella. The target thickness for the tip is less than 100 nm. Thinned lamellas should be investigated as soon as possible. Although the wedge shape is mechanically more stable, the thin tip starts deforming within a few weeks.

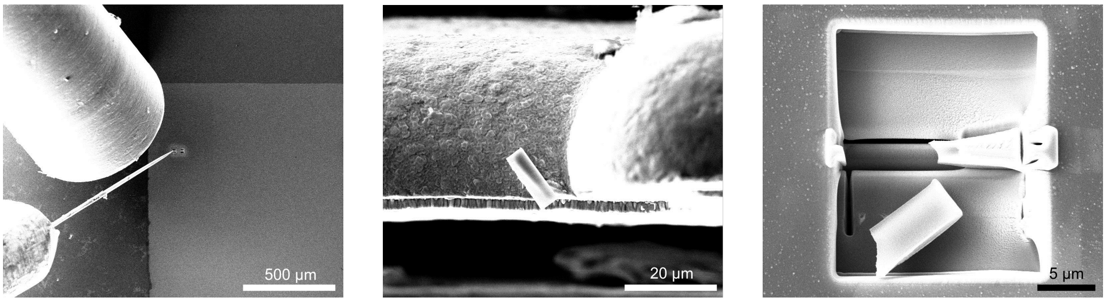

(a) (b) (c)

Figure 4.7: SEM images: difficulties while preparation (a) position of GIS needle and MM tip, (b) lost lamella after collision with TEM grid, (c) destroyed lamella after failed final cut.

Some of the challenges while preparation are shown in figure 4.7. The GIS needle is, while extracted for use, less than 300 nm apart from the MM tip. Their close proximity is shown in figure 4.7a.

4.3 Transmission Electron Microscopy

All TEM lamellas were investigated with a Jeol JEM2100F TEM at 200 keV. Measurements were performed preferably within a week after the thinning of the lamellas.

4.3.1 Imaging

The TEM used is equipped with two Gatan CCD cameras for imaging in TEM mode and two semiconductor detectors for imaging in STEM mode. From the TEM images, ITO and Al electrodes are clearly identifiable, as can be seen in figure 4.8. The glass substrate and the Pt protection layer are also distinguishable (figure 4.8a). Within the organic layer stack, for most samples no contrast difference is observable (figure 4.8b). The average atomic number of the materials in the layer stacks are almost identical to each other. In thicker areas of the wedge shaped lamella, a slight contrast difference is observable in TEM mode with the CCD camera. But in those areas, it is not possible to achieve high quality TEM images, as the pictures stay blurred.

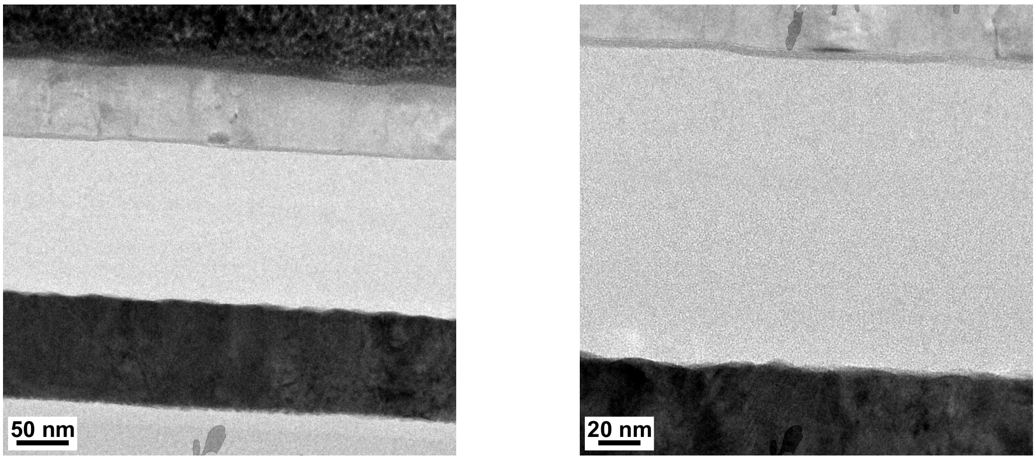

(a) (b)

Figure 4.8: TEM images of the cross section of an organic layer stack at the tip of the lamella

4.3.2 Energy Dispersive X-ray Measurements

The TEM used is capable of analyzing characteristic X-rays originating from the interaction of the electron beam with the sample using an energy dispersive Oxford X-MAX 80 SDD. The associated analytical software packet is called INCA, which was used for measurement control and data acquisition. The software allows the analysis of single points and multiple points arranged in a regular grid pattern, here called area scans. Acquired spectra were exported and analyzed with the software packet AXIL (analysis of X-ray spectra by iterative least squares) [66–68]. The file formats of these programs are not direct compatible. A small spectrum format conversion tool had to be developed for compatibility. This tool also automatically creates a batch command file to automatize spectrum fitting in AXIL.

To study the spatial distribution of elements across the device layers, EDX area scans were performed in STEM mode. The scans were planned and positioned using BF images. In the BF images of the inspected area, each white cross within a black square corresponds to a recorded spectrum.

To visualize the results, net peak counts for selected elements were combined into a pseudo image using a heat scale. The minimum count is coded black, while the maximum appears white. A scale with the particular minimum and maximum value is shown right to the respective element map. To combine the AXIL results from each spectrum and convert them into element maps, a program called ASR maps was used. Further combination of corresponding element maps into one image was carried out with the program Matrix Map Job [69].

For selected elements the distribution along the cross section is also displayed as line plots. The main interest is the distribution of elements along the cross section of the organic layers. The values for the line plots were calculated line by line and then averaged with corresponding standard deviation.

Additionally line plots for some elements were plotted together to visualize the layered structure of the sample. As net counts for the different elements vary strongly, each curve was normalized to its maximum for simultaneous presentation. The normalized plots clearly demonstrate the layered structure of the samples and help identifying possible fitting artifacts, e.g., as a result of increased spectral background.

The comparison of measurements from different lamellas is not expedient directly, as it is not possible to guarantee the same thickness for all measurements. This is enhanced by the preparation of wedge shaped lamellas, but remains also true for uniformly thinned lamellas. To correlate the measurements from different lamellas or different areas of one lamella a suitable normalization has to be applied. This could either be trough the copper (Cu) signal or an element present in the sample with known concentration. The Cu signal is caused by scattered electrons and bremsstrahlung X-rays, which excite the lift out grid.

When Bremsstrahlung X-rays hit the Cu grid to which the lamella is attached to, they can excite the Cu atoms, which leads to the emission of characteristic X-rays (X-ray fluorescence). Electrons scattered towards the Cu grid and with an energy high enough, also excite the Cu grid, again leading to the emission of characteristic X-rays. This Cu signal and Bremsstrahlungs X-rays are collected by the detector and contribute to the spectral background. The scattering of electrons from the sample depends on the average atomic number of the area of impact of the electron beam. The Cu signal is, therefore, related to the average atomic number at the measurement position. This can be seen in the element maps and is in good agreement with the TEM images taken at the lamellas' tip. Along the cross section there is a significant Cu signal for spectra recorded in the Al electrode, relatively few counts are observed for measurements in the organic layer and high counts for the ITO electrode. High electron scattering in the sample also leads to a larger overall spectral background, due to scattered electrons reaching the detector. The background difference is shown in figure 4.9. Two spectra from different sample areas are superimposed to demonstrate this effect. While the red spectrum was measured within the host layer, the blue one origins from the ITO contact. This also demonstrates the need for background removal during data treatment.

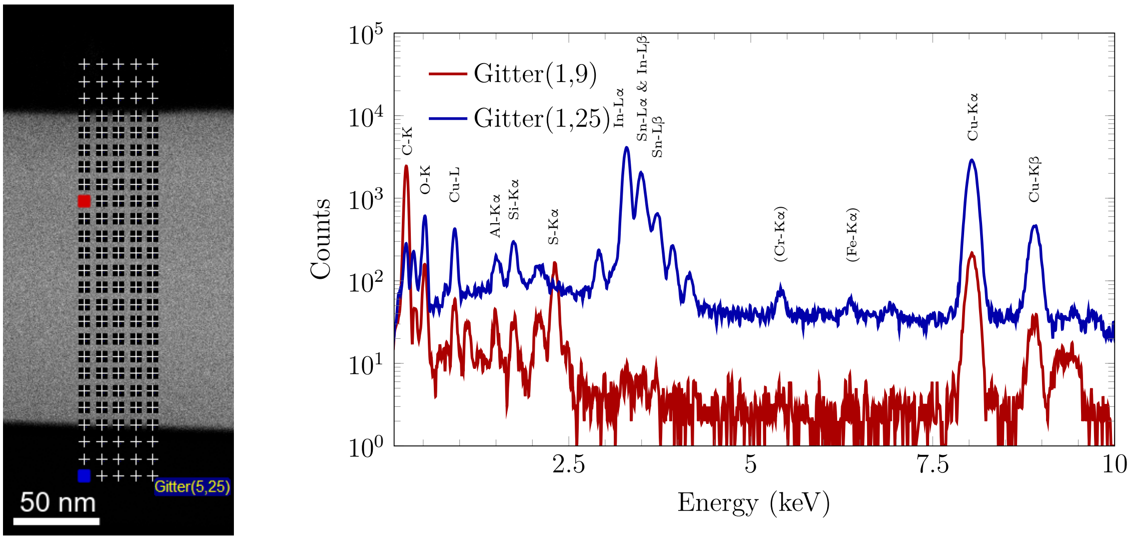

Figure 4.9: Comparison of a spectrum measured within the organic layers (red) to a spectrum measured in the ITO contact (blue).

4.4 Grazing Incidence X-ray Fluorescence and X-ray Reflectometry

XRF analysis of light elements is generally challenging due to the low fluorescence yield [70] and requires special analytic conditions, e.g., vacuum or helium-purge, optimized detectors, and suitable excitation sources [71–75]. As the XRR signal depends on the difference in electron density between neighboring layers, the analysis of layers with little difference in the mean atomic number might not be feasible. The prospect of information on interfaces and element distribution, which a combinded GIXRF/XRR may provide, lead to the decission to perform test measurements at Atominstitut, TU Wien [59, 60]. The architecture of the samples used for the test measurements was identical to those analyzed by TEM except for the Al contacts. The 50 nm thick Al contacts would absorb the S signal completely (transmission of about 10^{-9}) and distort the angle curves.

Promising angle curves could be obtained from these samples. However exact modeling to get quantitative results was not possible due to the ITO contacts below the organic layers, which partially intersect the inspected area. Therefore samples without the ITO electrodes were fabricated.

Further measurements were performed using a PANalytical Empyrean diffractometer at Röntgenzentrum, TU Wien, in cooperation with Atominstitut, TU Wien. The instrument with a θ - θ goniometer offers beam optics and detectors for XRR. The Cu long fine focus HR X-ray tube was operated at 45 kV and 40 mA. A hybrid monochromator, consisting of a parabolic multilayer mirror and a channel-cut germanium (220) crystal, provides almost pure $K\alpha_1$ radiation with low divergence. In the horizontal plane the beam is limited by a mask with a width of 10 mm, which is positioned before the monochromator. The beam height is narrowed by a divergence slit (50 µm). The diffracted beam was measured with a PIX-cel3D area detector in receiving slit mode. For the simultaneous acquisition of XRF spectra an energy dispersive X-ray detector is added to the diffractometer. The Amptek XR-100SDD with an 8 µm beryllium entrance window and a silver collimator (4 mm diameter) is positioned approximately 3 mm above the sample. The measurement in the diffractometer were performed in normal atmosphere.

The measured GIXRF/XRR angle curves were processed using the software package Java grazing incidence X-ray analysis (JGIXA) for model simulation and fitting [76]. The software is capable of an analysis of simultaneously recorded angle curves. Beside the benefit of circumventing the ambiguities both techniques exhibit, when used solely, the software also provides a number of different algorithms for optimization. Instrument parameters were determined from measurements of reference samples and kept invariant for the simulation of the samples. A possible thin water layer on top of the layer stack due to exposition to air was considered according to [52, 77, 78].

4.5 X-ray Photoelectron Spectroscopy

As TEM-EDX and GIXRF measurements only provide information on the elemental composition but not on the binding state, XPS measurements were performed for certain samples.

XPS measurements were performed with an ESCALAB 250 Xi instrument from Thermo Fisher. It is equipped with a monochromatized X-ray tube with Al anode and an X-ray tube with Mg/Al dual anode. The energy of the photoelectrons is determined with a hemispherical analyzer. Electrons are detected using a channeltron. The instrument is additionally equipped with an argon (Ar) sputter gun, which is able to use Ar ions and Ar clusters. The sputter gun can be used to clean the sample surface or to remove sample material for depth profiling. This process is referred to as etching.

Beside a survey spectrum, scans for C and S were recorded. To investigate the distribution of elements, especially of S, beneath the host layer, depth profiles using the Ar sputter gun were recorded. The first scans were performed on the surface. The sample was then bombarded with small Ar clusters with an energy of 4000 eV for 20 s. The next scan was delayed 30 s after each etch. Altogether 15 levels were measured.

Due to the low conductivity of the sample material, the flood gun was used for charge compensation. Sample height was adjusted to achieve maximal count rate. Energy intervals measured for C and S were determined with test measurements before the depth profiling.

5 Results

In this chapter the different sample types and their characterization are presented. For each sample type its composition, nominal layer structure and preparation is described, followed by the analytical results.

5.1 Iridium Based Emitter

First experiments were performed using samples with an emitter material containing Ir. These samples were dedicated to test sample preparation and the detectability of Ir by TEM-EDX.

The device architecture of the first sample set is shown schematically in figure 5.1. Layer thickness and composition are specified in table 5.1

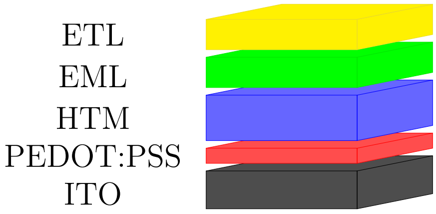

Figure 5.1: Schematic device architecture of samples with vapor deposited Ir based emitter.

All layers except the PEDOT:PSS (poly(3,4-ethylenedioxythiophene) polystyrene sulfonate) were vapor deposited. The PEDOT:PSS layer was spin coated and annealed for 10 min at 180 °C. The hole transport material (HTM) is an aryl substituted monoamine. The p-dopant enhances the hole injection. The host is an electron transporting material based on a triazine unit. The electron transport material is also triazine based and suitable for a wide range of different OLED stack architectures. The emitter molecule is a tris(2-phenylpyridine)iridium(III) (Ir(ppy)$_3$) derivative. The unusual high emitter molecule concentration of 50 % was chosen to facilitate Ir detection. Due to the preparation of TEM lamellas using FIB, Pt and Ga are also present in the sample. Pt origins from the deposited protection layer and Ga from implanted ions during FIB milling. Unfortunately the Ir-L lines are in a similar energy range as the Ga-K and the Pt-L lines. Such line overlaps can significantly increase detection limits.

Table 5.1: Layer sequence and thicknesses of samples with vapor deposited Ir based EML

ETM + Liq	10 nm
ETM	30 nm
90 % host + 10 % emitter	20 nm
50 % host + 50 % emitter	20 nm
HTM	40 nm
95 % HTMs + 5 % p-dopant	20 nm
PEDOT:PSS	20 nm
ITO	50 nm

In comparison to the vapor deposited samples, samples with solution processed EML were investigated. The schematic device architecture is shown in 5.2 and materials and layer thicknesses are quoted in table 5.2

Figure 5.2: Schematic device architecture of samples with solution processed Ir based emitter.

For this samples all layers except the ETL were spin coated. The buffer layer consists of a conductive polymer, which enhances the hole injection from the ITO anode. The HTL is based on a copolymer, which was spin coated from a toluene solution and annealed for 30 min at 220 °C. It consists of a diamine backbone with cross linking groups attached. During annealing, the polymer chains are thermally

Table 5.2: Layer sequence and thickness of samples with solution processed Ir based EML

ETM + Liq	10 nm
ETM	30 nm
host1 + host2 + emitter	60 nm
HTM	40 nm
buffer	20 nm
ITO	50 nm

cross linked via these groups. The EML consists of two host materials and a soluble derivative of Ir(ppy)$_3$ as emitter molecule. One host enhances the electron transport in the layer with a triazine unit and the second host is a wide band gap material. The EML was annealed for 10 min at 150 °C. The ETL consists of the same materials as for the predominantly vapor deposited samples and was also vapor deposited for the solution processed samples.

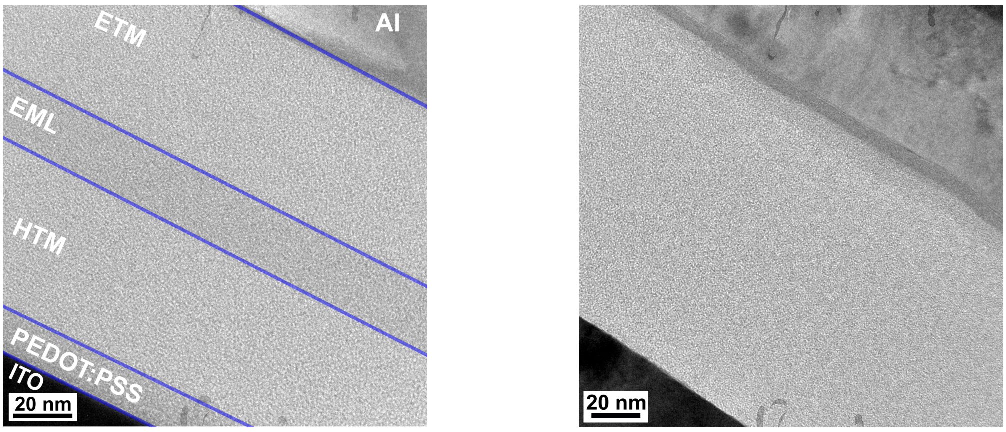

(a) (b)

Figure 5.3: TEM images of the organic layer stack of samples with vapor deposited emission layer (a) and solution processed emission layer (b).

TEM images of lamellas fabricated from vapor deposited and solution processed samples are shown in figure 5.3. These images were recorded with a CCD camera. For the vapor deposited sample in 5.3a, the Ir rich portion of the EML and the PEDOT:PSS layer can be discriminated from the remaining organic layers. Contrariwise no contrast difference is visible for the solution processed sample, as can bee seen in 5.3b.

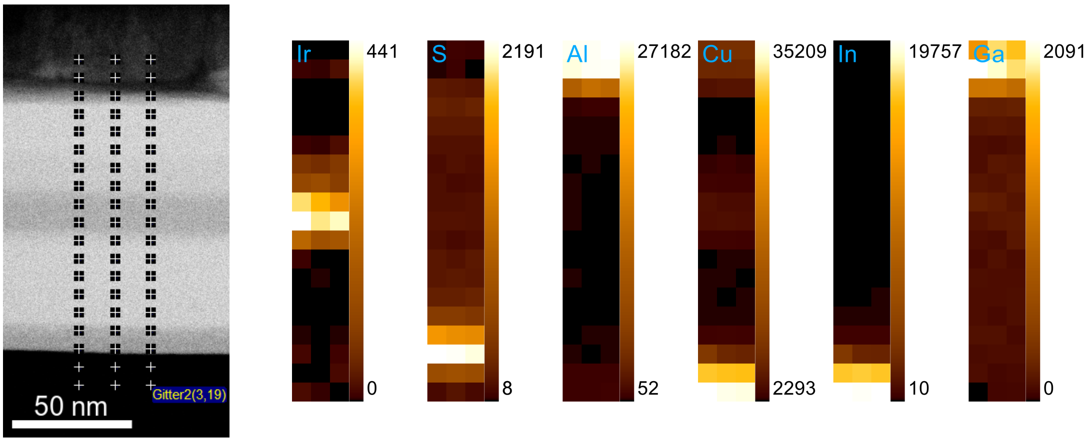

Figure 5.4: Left: BF image of the investigated area with grid of measurement points, right: element maps for selected elements of a sample with vapor deposited EML

In the BF images of a thicker region of the lamella, taken in STEM mode, also the layer with the lower emitter concentration can be distinguished, as shown in the left hand side image in figure 5.4. The element maps on the right in figure 5.4 reveal, that EDX analysis clearly identifies the layers containing Ir. The difference in emitter concentration in the EML is also visible. The change in the mean atomic number by the Ir containing molecule in comparison to the strictly organic materials can also be seen in the Cu signal.

Figure 5.5a shows the Ir distribution along the device's cross section for the vapor deposited sample. The values for the line plots were derived from the Ir net counts, which were averaged for each line of the area scan. The Ir containing layers are clearly identifiable through the distinct Ir counts. Even the concentration difference within the EML is observable. In the ETL, HTL and the layer containing PEDOT:PSS no significant Ir counts could be detected. In figure 5.5b the layered structure of the device is visualized plotting the normalized net counts for certain elements along the device cross section. While Al and Ga are only present in the Al electrode, indium (In) counts are only significant for the ITO electrode. As the Cu signal is a measure for the mean atomic number of the particular measurement point, it is significant in the Al electrode and has a small bump in the Ir rich layer. The maximum Cu signal can

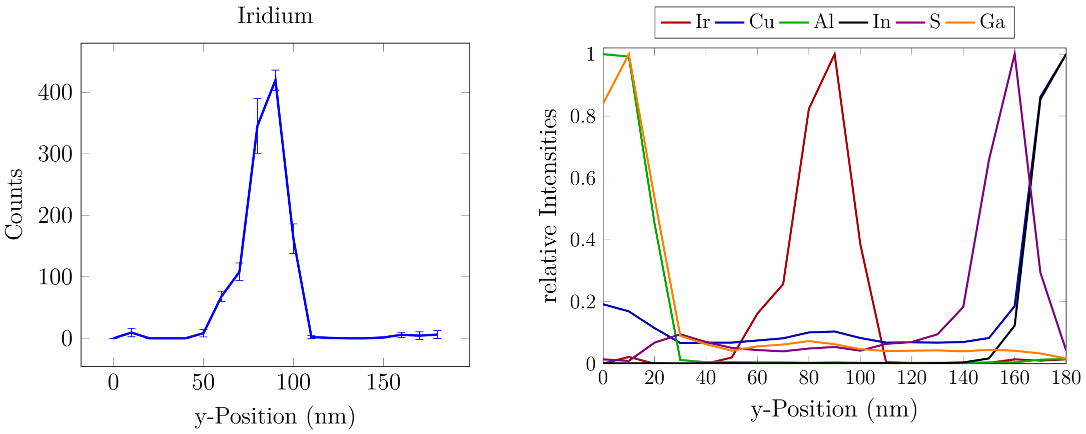

(a) (b)

Figure 5.5: (a) averaged Ir distribution along the cross section (y=0 corresponds to the Al contact, y=180 to the ITO contact), (b) normalized line plots for the elements Ir, Cu, Al, In, S and Ga along the cross section for a sample with vapor deposited EML.

be found within the ITO electrode. The S concentration of the PEDOT:PSS layer is also visible as a peak.

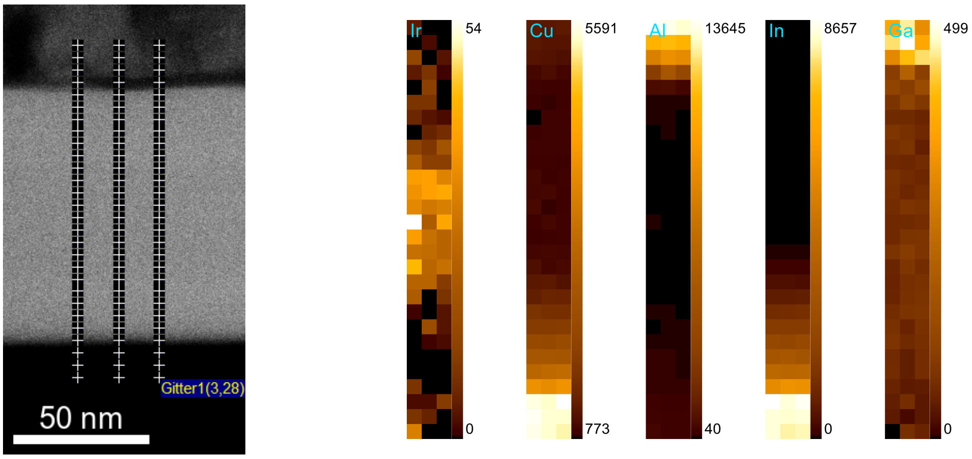

Figure 5.6: Left: BF image of the investigated area with grid of measurement points, right: element maps for selected elements of a sample with solution processed EML.

In the BF image (left image of figure 5.6) the EML is slightly visible, but clearly less than in the layer with the high emitter concentration of the sample set with vapor deposited EML. The concentration of Ir in the EML of the samples with solution processed EML is close to the one in the layer with lower emitter concentration of the samples with vapor deposited EML. The contrast in the BF images matches that.

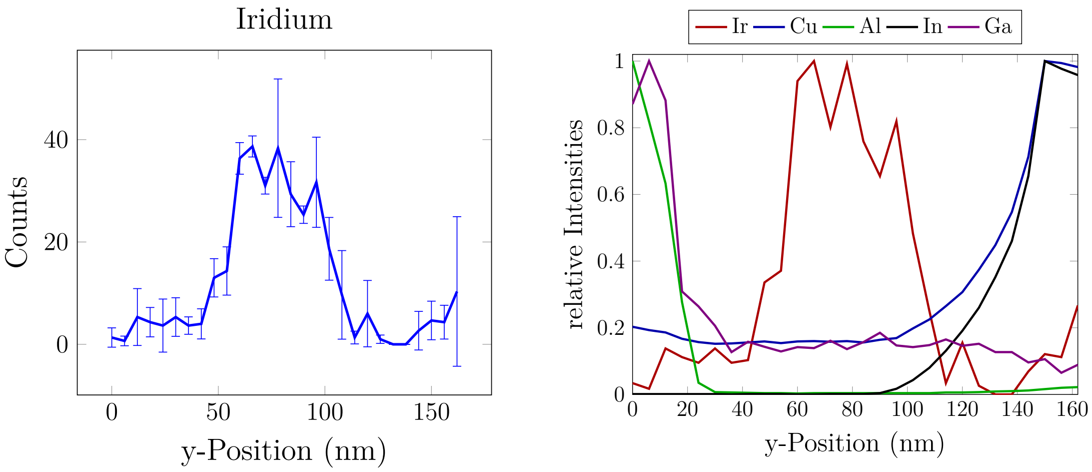

(a)

(b)

Figure 5.7: (a) averaged Ir distribution along the cross section (y=0 corresponds to the Al contact, y=162 to the ITO contact), (b) normalized line plots for the elements Ir, Cu, Al, In and Ga along the cross section for a sample with solution processed EML.

For the samples with solution processed EML the Ir concentration is not artificially high as for the vapor deposited sample, but in a range which is typical for phosphorescent emitters used in OLED. The relatively low concentration of about 1 % in the EML, corresponds to small net counts for Ir in the EDX analysis. The maximum net count for Ir is only 54, as can be seen in the element map for Ir in figure 5.6. The low Ir counts also show relatively high deviations, leading to distinct error bars in the Ir line plot across the layers in figure 5.7a. Significant Ir counts could only be detected for the EML. The plot of the normalized net counts for selected elements again reveals the electrodes and the variation in the mean atomic number by the means of the Cu signal (figure 5.7b).

The standard approach is to evaluate the L lines for Ir. As there are overlaps with the K lines of Ga and the L lines of Pt, it is also helpful to investigate the M lines of Ir. The peak at 1.98 keV is clearly visible in the spectra and it is possible to discriminate it from the Pt M lines. A comparison of the net Ir counts of the M-peak to those of

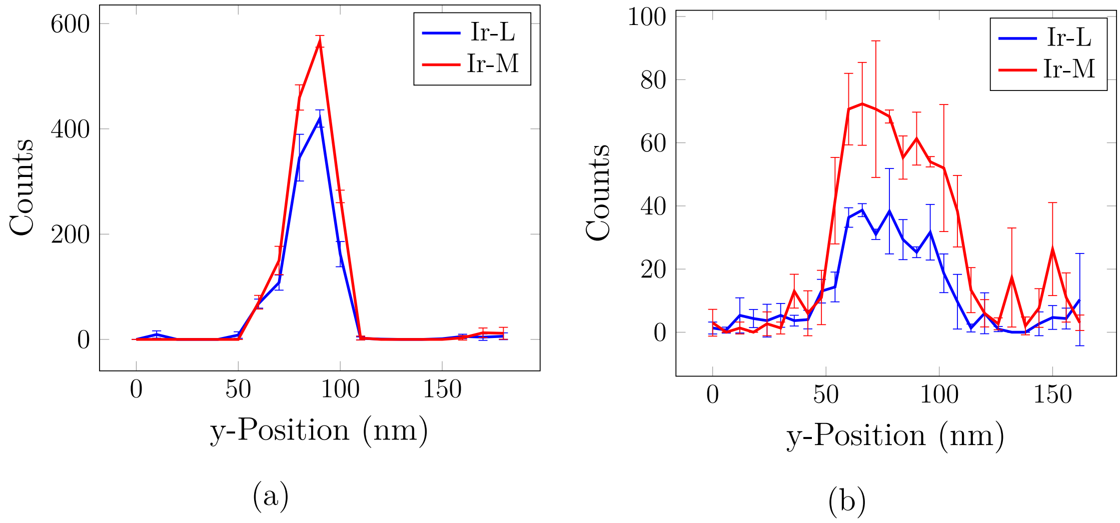

(a)

(b)

Figure 5.8: Comparison of the Ir net counts for L and M lines of (a) a sample with vapor deposited EML and (b) a sample with solution processed EML.

the L-peak is shown in figure 5.8. For samples with vapor deposited EML the plot of the M lines has a higher maximum and lower deviation within lines of the scans. The shape of both curves is almost the same. For the sample set with solution processed EML the evaluation of the M lines also yields higher net Ir count, but there is a higher deviation within the scan leading to higher error bars. The overall low signal does not allow for exact evaluation as it is close to the lower limit of detection. A diffusion of Ir due to the preparation process cannot be detected in this case. In the ITO region of the sample the net Ir counts rise, which is most likely due to an in general higher background at the low energy region of the spectrum. Aside from this false positive Ir signal the evaluation of the Ir M lines is a valuable approach.

Due to the challenges with the detection of Ir in the low concentration used in OLED devices, a material based on a more suitable element was chosen for further investigation. For the regular concentration of the emitter material, the maximum value of net counts was only about 50 counts. A significantly lower Ir concentration in the layer beneath the solution processed EML, as would be expected from intermixing or diffusion effects, would therefore be hard to detect.

5.2 Small Molecule Host

In order to study the differences between solution processed and vapor deposited samples a material was chosen, which can be used with both preparation methods. A small molecule host material containing S was used. In the previous section, S was detected within the PEDOT:PSS layer. A lower S concentration should be detectable, in comparison to Ir, as there are no other element lines within the energy region of S-K lines present in the sample. The overlap of molybdenum-L lines with S-K lines is no concern for samples used.

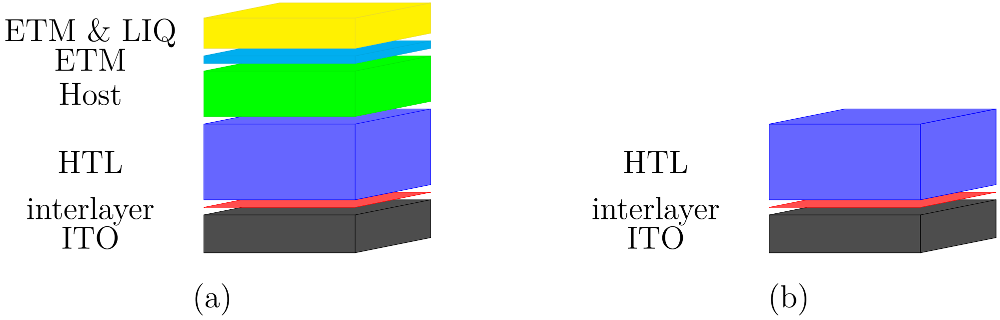

(a)

(b)

Figure 5.9: Schematic device architecture of (a) samples with SM host material and (b) control sample with only HTL.

The samples used were so called "electron only" devices. Single carrier devices allow the study of energy transfer processes in organic materials. In the case of an electron only device, a hole blocking layer prohibits the injection of holes into the HTL. Schematic device architecture is shown in figure 5.9. The multilayer structure consists of 100 nm HTL, 60 nm host and 50 nm ETL between the 50 nm thick ITO anode and the 100 nm thick Al cathode. The very thin (monolayer) interlayer blocks hole injection into the HTL. Additionally a sample with solely 100 nm HTL between the electrodes was investigated.

As HTL material served a copolymer with a molecular weight of 8800 g/mol. It consists of alternating monomer units, shown in figure 5.10a. The substituents on the amine units are either aryl or vinyl units. The vinyl groups are responsible for cross linking of the polymer chains. The R groups on the indenofluorene consist of alkyle chains and improve solubility in toluene. The polymer was spin coated from a toluene solution with a concentration of 18 mg/mL. The rotation speed was adjusted to obtain the desired thickness of 100 nm and measured with a Dektak profilometer,

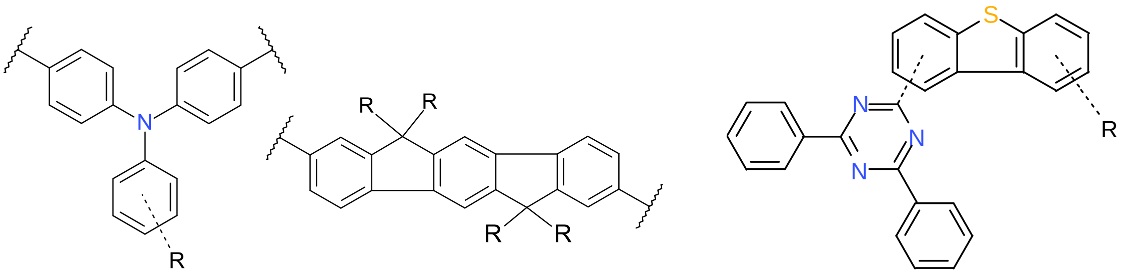

(a) (b)

Figure 5.10: Structure of (a) the monomers forming the polymer for the HTL, (b) the small molecule host material.

with an expected accuracy of ±3 nm. The resulting layer was annealed for 30 min in a nitrogen glove box at 200 °C, to cross link the polymer chains thermally. The ETL was deposited by thermal evaporation in a Lesker tool at a base pressure of around 10^{-6} mbar. The evaporation rate of 0.3 nm/s was controlled with a quartz crystal microbalance, which was calibrated for different materials using thickness measurements with a Dektak profilometer. The small molecule host used is a standard material for combination with green or red triplet emitters. It consists of a triazine bonded to a dibenzothiophene unit, as shown in figure 5.10b. The substituent R is a heterocyclic aromatic unit. This molecule can either be vapor deposited or solution processed. Vapor deposition of the host layer was also performed in the Lesker tool. The solution processed host layer was spin coated from a toluene solution and afterwards annealed for 10 min at 110 °C.

From each of these three sample types two TEM lamellas were fabricated. In the TEM images in figure 5.11 the ITO and Al electrodes are clearly identifiable. The glass substrate beneath the ITO anode and the platinum protection layer, which was added during FIB milling, are also clearly distinguishable. For the different organic layers within the layer stack, no contrast difference is observable at the tip of the lamella. In addition no visible differences between samples with solution processed host layer and those with vapor deposited could be observed (see figure 5.12).

Figures 5.13 and 5.15 show BF images of the measurement area and the corresponding element maps. The spatially resolved EDX analysis reveals the highest S net counts in the host layer for both sample types. This is an expected result, as only the host material contains S. In the vapor deposited ETL material, no significant S

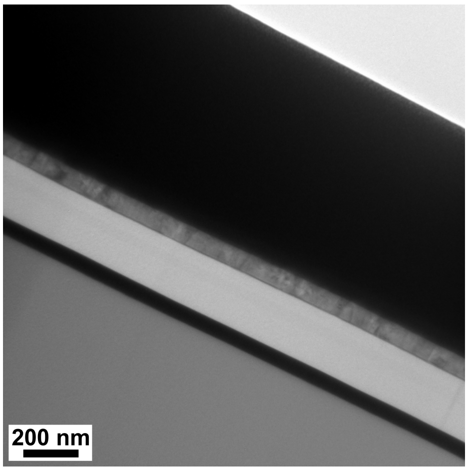

Figure 5.11: TEM-image of a lamella of sample set 3 with slight contrast difference within the organic layers. Due to the thickness the image is blurry.

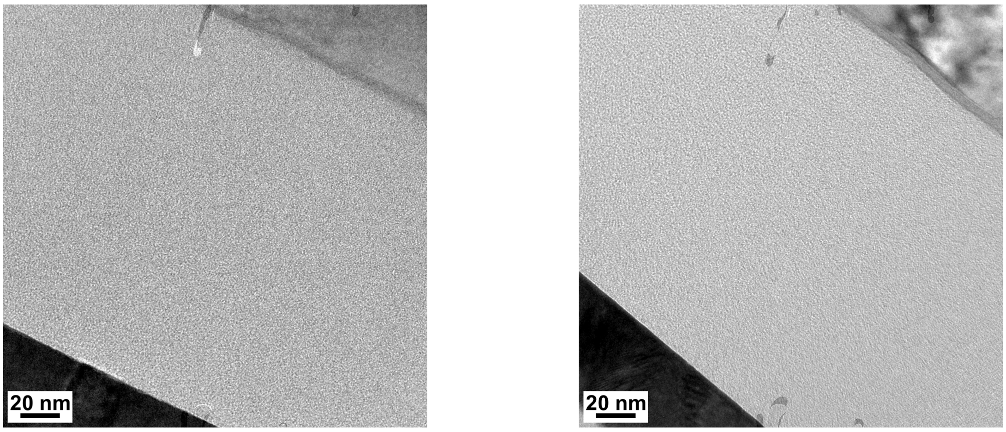

(a)

(b)

Figure 5.12: TEM images of the organic layer stack of samples with (a) solution processed host and (b) vapor deposited host.

counts were detected, again for both sample sets. For samples with a vapor deposited host layer, there are also no significant S counts in the HTL.

As visualized in figure 5.14, for samples with a solution processed host layer, a significant S content was detected in the HTL. The S counts are evidently lower compared to those in the host layer, but they can be found throughout the whole HTL. The distribution of S along the cross section is obtained from the EDX area scans. The mean value with its standard deviation is calculated for each line of the scan.

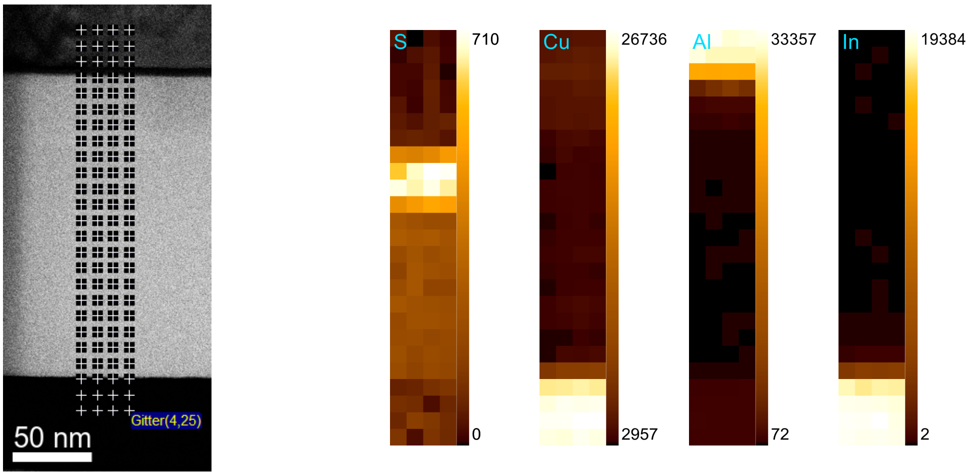

Figure 5.13: Left: BF image of the investigated area with grid of measurement points, right: element maps for selected elements of a sample with solution processed host layer.

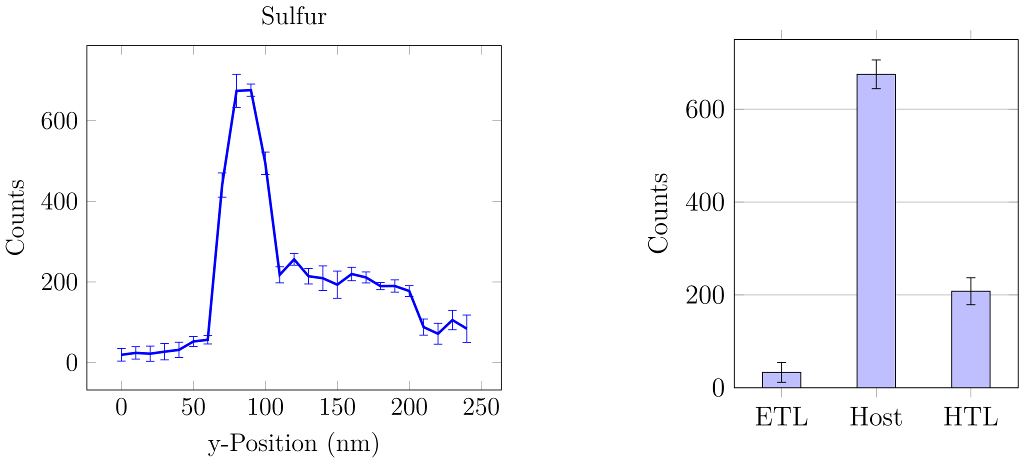

Figure 5.14: Left: averaged S distribution along the cross section (y=0 corresponds to the Al contact, y=240 to the ITO contact), right: averaged S counts from the segmented area scan of a sample with solution processed host layer.

The normalized line plots show the distribution for certain elements along the cross section for samples with solution processed host layer in figure 5.17a and for samples with vapor deposited host layer in figure 5.17b. For these plots also the average over a line in an area scan was calculated. Additionally the plot for each element was normalized to its maximum to take the high difference in net counts between the elements into account. The normalized line plots visualize the layered structure along the cross section. Al and In are again only present in the respective electrodes. The Cu signal shows its lowest in the organic layers, a little elevated in the Al contact and reaches its maximum within the ITO contact, as it is correlated with the average atomic number of the measured point.

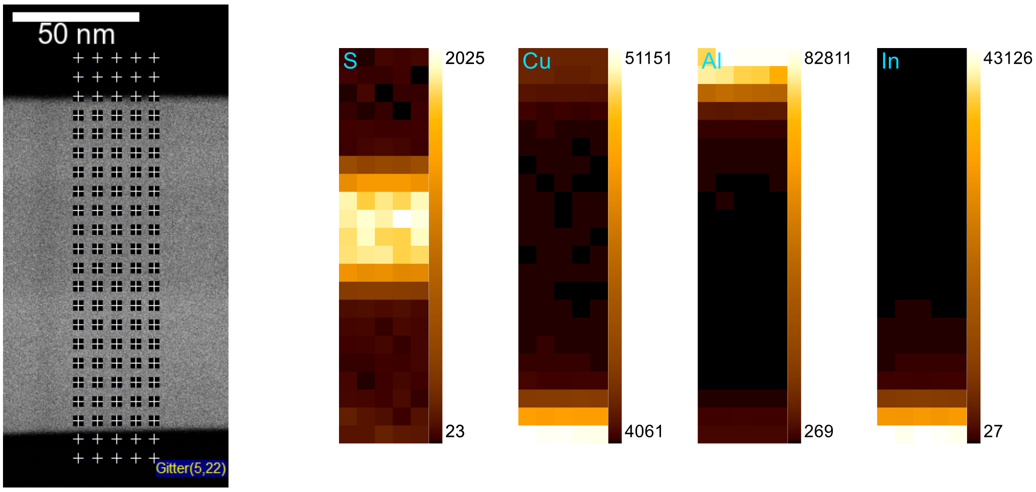

Figure 5.15: Left: BF image of the investigated area with grid of measurement points, right: element maps for selected elements of a sample with vapor deposited host layer.

To compare the results of both sample sets, an average S count for each layer was calculated with two different approaches. For the first, the measurement points were assigned to the corresponding layer using the BF images of the measurement areas. For each of the three layers, a mean S net count was calculated from the net counts of the respective spectra. Data from transition points was excluded. The results for each layer are shown in the bar chart on the right of figure 5.14 for the sample with solution processed host layer and in the right hand side of figure 5.16 for the vapor deposited host. The second approach was to measure line scans along the center of a layer and parallel to the contacts for all three organic layers and calculate an averaged net S count for each layer.

A direct comparison of the counts is not reasonable, as it is not possible to guarantee the same thickness for measurement areas from different lamellas. For correlation, the counts for a certain element were normalized to the its highest counts. For S these were always found within the host layer, for Cu and In always in the ITO contact.

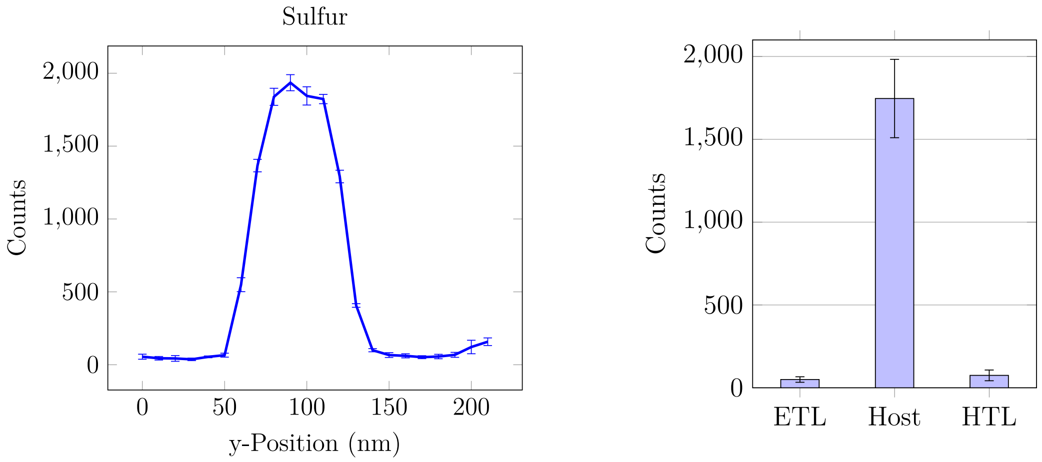

Figure 5.16: Left: averaged S distribution along the cross section (y=0 corresponds to the Al contact, y=210 to the ITO contact), right: averaged S counts from the segmented area scan of a sample with vapor deposited host layer.

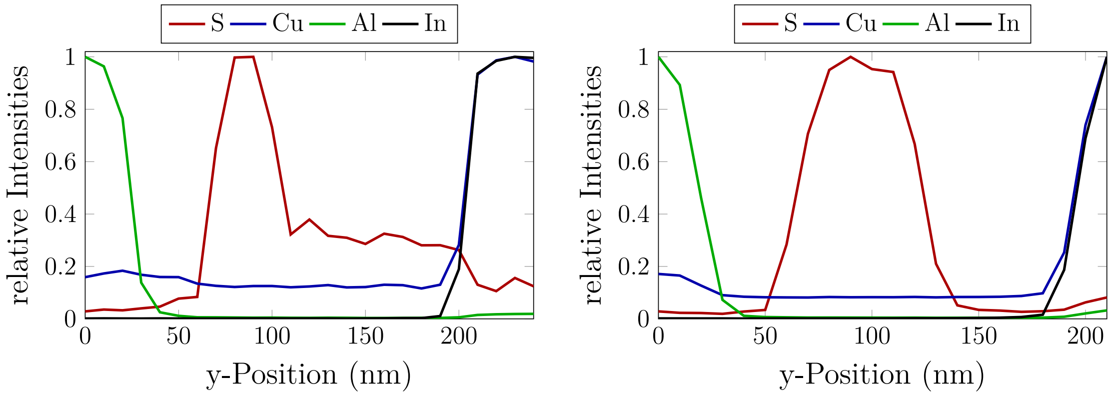

(a)

(b)

Figure 5.17: Normalized line plots for the elements S, Cu, Al, and In along the cross section of a sample with (a) solution processed host layer and (b) vapor deposited host layer.

This semi-quantitative approach allows for the comparison of S counts in ETL and HTL for measurements on different lamellas.

Both approaches show a very similar result, which is shown in figure 5.18 for the segmented area scans and in figure 5.19 for the line scans. Only the samples with solution processed host layer show a significant S count aside from the host layer.

Since for both sample types the same materials were used and the only difference was the manufacturing process of the host layer, it is reasonable to expect that the penetration of S into the HTL is caused by the solution-based deposition of the host layer. This may disturb the strict layer sequence in a way to cause the previously mentioned performance differences.

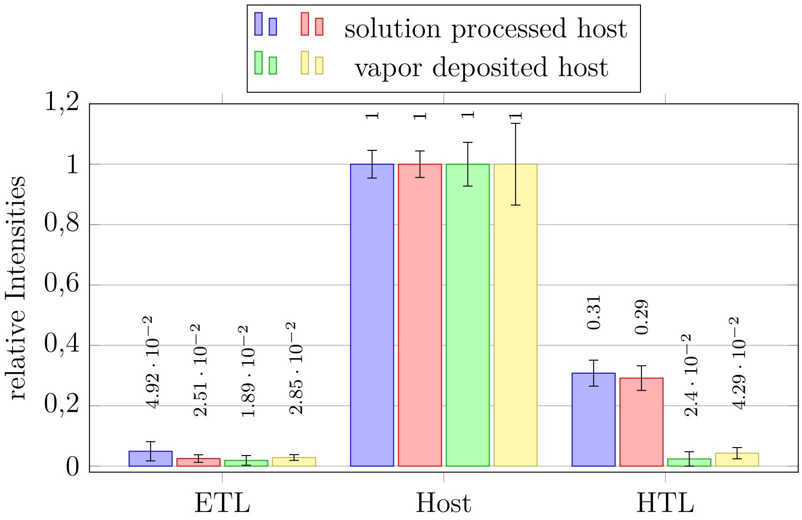

Figure 5.18: Comparison of normalized S net counts within the organic layers of samples with differently prepared host layer, derived from fragmented area scans.

The measurement of the lamellas prepared from the HTL only sample, showed no significant S counts. A possible S residue from the used solvent toluene would therefore lie beneath the detection limit of TEM-EDX, which ranges from 0.1 % to 1 % depending on sample composition and thickness [43].

To compare the spatial distribution of S along the cross section, the normalized line plots for S were superimposed in figure 5.20. The four area scans were measured on four lamellas, two lamellas from samples with solution processed host and samples with vapor deposited host layer each. All of the area scans were positioned within a BF image of the lamella. To compare the different area scans, these measurement positions have to be aligned. The alignment was achieved by identifying the transition from the ETL to the host layer as a reference point. An error in the range of the EDX area scan resolution, here either 10 nm in figure 5.20a or 5 nm in figure 5.20b, can remain. For equally prepared samples, the scans show a good agreement. However, when comparing the scans of samples with differently prepared host layer, the host

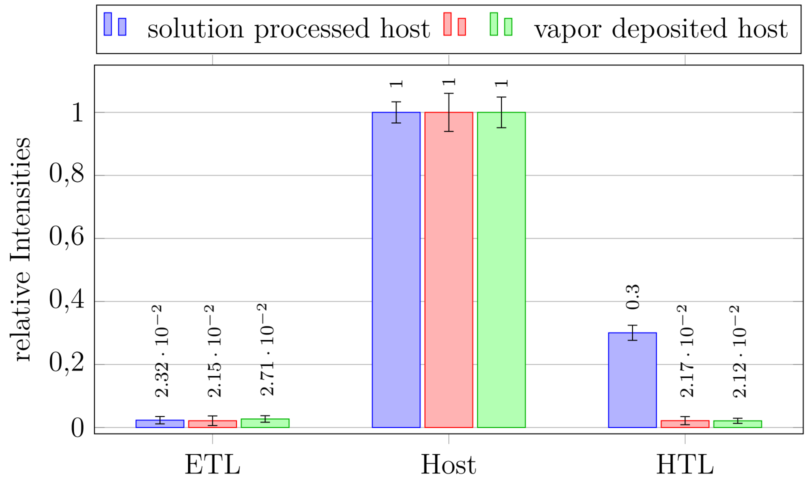

Figure 5.19: Comparison of normalized S net counts within the organic layers of samples with differently prepared host layer, derived from line scans area scans.

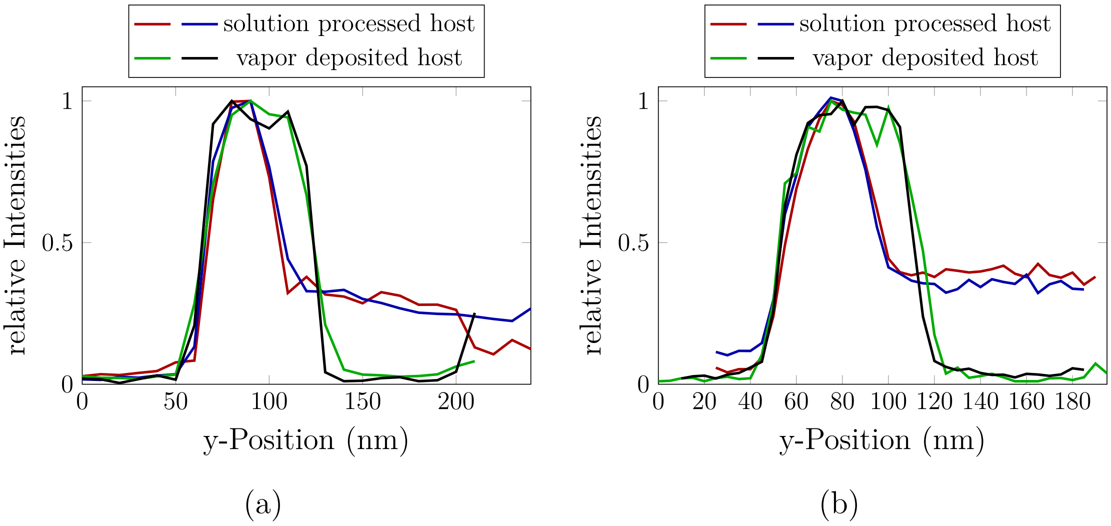

(a)

(b)

Figure 5.20: Comparison of the normalized S distribution along the sample's cross section from different (a) 10 nm×10 nm and (b) 10 nm×5 nm area scans of samples with differently prepared host layer.

layer for samples with solution processed host layer is sinificantly thinner than the corresponding layer for the samples with vapor deposited host. The already mentioned difference in the S counts in the HTL is also clearly visible. Only in the HTL beneath the solution processed host layer a significant S signal was detected. From these data, it appears as if S from the host layer has moved partially to the HTL.

It remains unclear which mechanism causes the differences in S distribution. But it seems that the annealing of the HTL to cross link the materials side chains, does not make the resulting layer resistant enough to withstand the deposition of the solution processed host layer unaltered.

5.2.1 Grazing Incidence X-ray Fluorescence and X-ray Reflectometry

For the combined GIXRF/XRR measurements multilayer and single layer samples were fabricated on SiO_2 substrates without electrodes. The single layer samples of buffer, HTL, vapor deposited and solution processed host were used as reference samples. The multilayer stacks consisted of two or three layers, respectively buffer/HTL and buffer/HTL/host. While buffer layer and HTL were solution processed for all samples with a thickness of 20 nm each, the host layer was vapor deposited or solution processed and had a thickness of 60 nm. Therefore in total 7 different sample types were investigated.

While the spin-coated host layer covers the whole substrate (30 mm×30 mm), the vapor deposited host layer only covers an area of 16 mm×16 mm in the middle of the substrate, due to the shadow mask used in the thermal evaporation process. For the GIXRF/XRR measurements, beside the fabrication of organic layers and layer stacks, no further sample preparation is required. The materials used were, beside the buffer material, the same as for the samples for TEM-EDX measurements. As buffer a doped, conductive polymer was spin coated from a toluene solution with a concentration of 8 mg/L and annealed for 30 min at 200 °C. The HTL was also solution processed, but in contrast to the samples for TEM-EDX measurements, from a toluene solution with an concentration of 8 mg/mL. The differences in concentrations are necessary to achieve the different layer thicknesses. The host layer was again either solution processed or vapor deposited. The procedure was the same as for the TEM-EDX samples. The samples differ in the used substrate and the missing ETL and Al contact. The use of a different substrate was necessary as the structured ITO may have caused unwanted effects at the contact edges.

Single Layer Samples

Single layer samples with either solution processed host or vapor deposited host and a thickness of 60 nm have been measured with GIXRF and XRR.

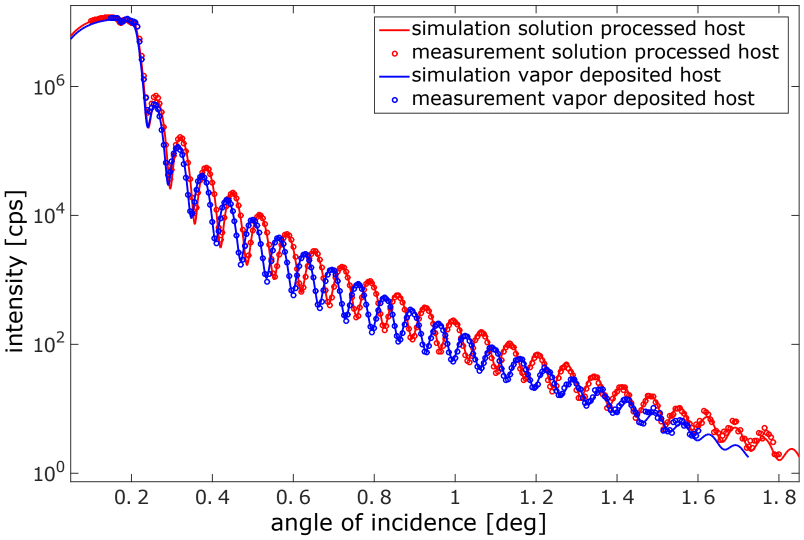

Figure 5.21: XRR curve of differently prepared host layers (60 nm).

The S GIXRF signals in figure 5.22 only differ slightly in intensity and position of the maximum. This is likely caused by some variance of layer thickness between the two samples. A significant difference can be found in the XRR angle curves (see figure 5.21) in oscillation width, which is broader for the solution processed host layer. Oscillation width is influenced by layer thickness. The Si bulk signal from differently prepared samples shows little difference and is displayed in figure 5.23. The fluctuations before and after the steep increase in intensity are caused by the interference of the Si signal with the layer above the substrate.

Results of the sample modeling with JGIXA can be found in tables 5.3 and 5.4. The calculated thickness of the host layers corresponds well with the expected value of 60 nm. The vapor deposited host layer appears to be slightly thicker. Furthermore, the surface roughness is higher for the vapor deposited host. For the density, no significant difference between the differently prepared host layers could be found.

From the materials used, only the host material contains S. As the HTL is solution processed from a toluene solution, a possible S residue was investigated analyzing the HTL single layer sample, with a thickness of 20 nm, in a special low Z TXRF

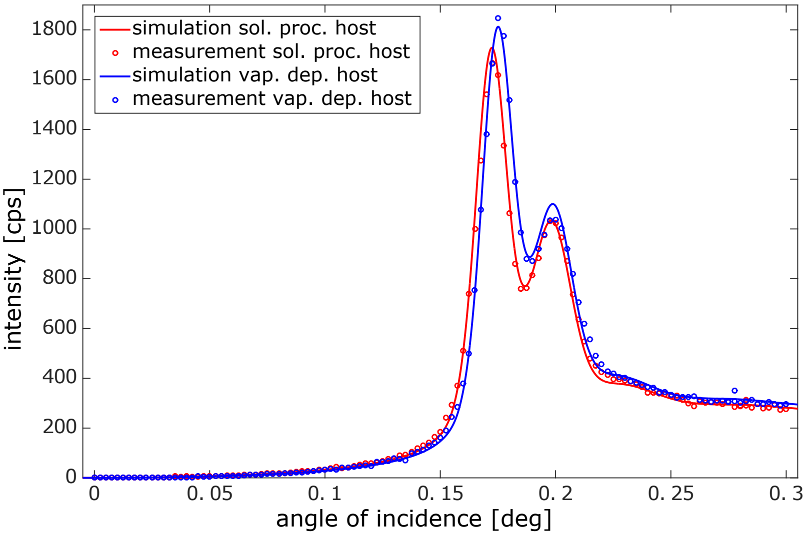

Figure 5.22: S-Kα GIXRF curve of differently prepared host layers (60 nm).

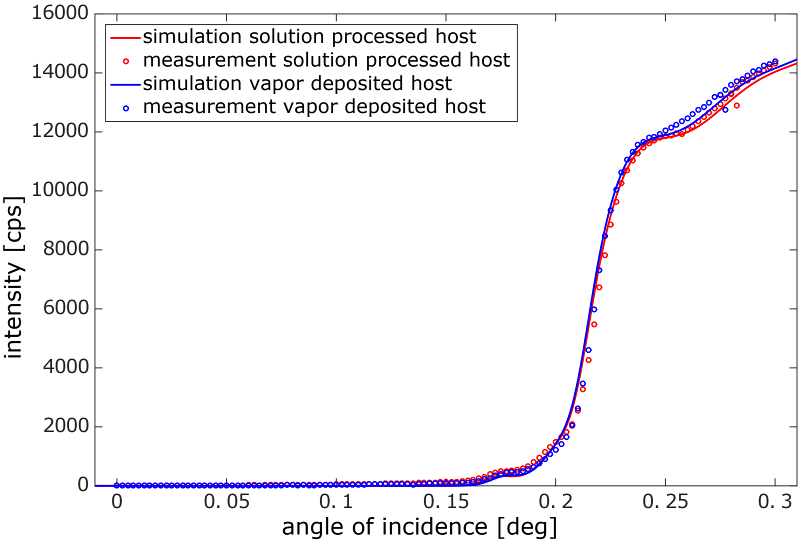

Figure 5.23: Si-Kα GIXRF curve of differently prepared host layers (60 nm).

spectrometer [79]. The set up is equipped with a 1.9 kW chromium anode X-ray tube with long fine focus, a W/C multilayer monochromator and a Ketek VIAMP SDD with a 300 nm thick polymer window (Moxtek AP3.3). S could be detected, but from the very low signal in this sensitive set up the estimated amount is under 0.1 %. This value lies below the TEM-EDX detection limits. Due to low count rates from thin samples, these limits typically lie in the range from 0.1 % to 1 % [43].

Table 5.3: Results of the vapor deposited host single layer sample

Layer	Thickness (nm)	Density (g/cm^3)	Roughness (nm)
H_2O	1.08	0.49	1.06
Host	64.26	1.24	4

Table 5.4: Results of the solution processed host single layer sample

Layer	Thickness (nm)	Density (g/cm^3)	Roughness (nm)
H_2O	0.21	0.4	0.86
Host	62.61	1.2	2.64

Multilayer Samples

While buffer layer and HTL were solution processed for all multilayer samples, the host layer was either vapor deposited or spin coated. In comparison to the single layer samples, the XRR angle curves in figure 5.24 show a clearer difference for samples with differently prepared host layer. The oscillation for the solution processed host is even. For the vapor deposited host the XRR angle curve shows a more irregular pattern. The irregular oscillation is the result of interference between the signals of the different layers. For the even pattern, the superposition of different signals is such that the signal altogether appears even. The amplitude of the oscillation declines faster with increasing incidence angle for the vapor deposited host sample. The decline of the oscillation's amplitude and intensity is linked to surface and interface roughness.

The S-Kα angle curves in figure 5.25 display different S features at the shoulder of the peak. These features are influenced by the different S distribution in the layers beneath the host layer. The Si-Kα curves in figure 5.26 show again the typical shape for a bulk signal. As for the single layer samples, differences between the Si-Kα curves of both samples are small. Fluctuations around the steep increase are caused by the interference of the primary beam with the radiation reflected by the organic layers and the substrate.

For solution processed OLEDs, the formation of an interface layer of finite thickness

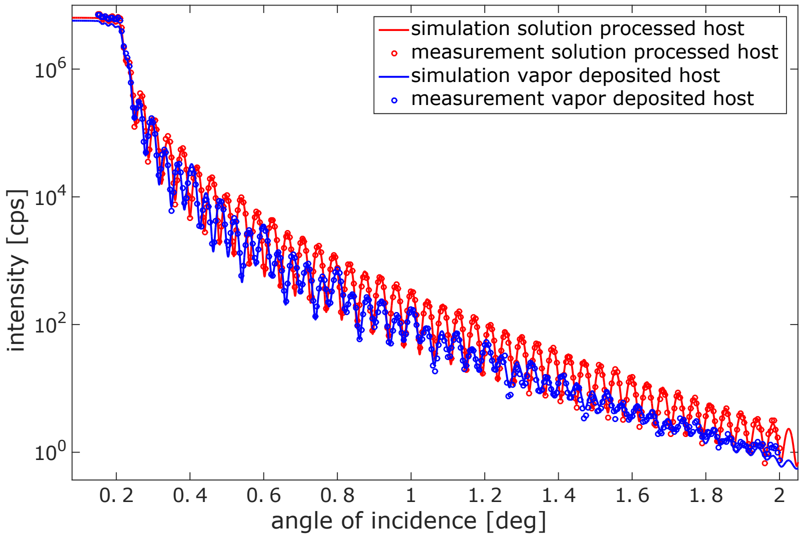

Figure 5.24: XRR curve of layer stack samples (buffer 20 nm/HTL 20 nm/host 60 nm) with differently prepared host layers.

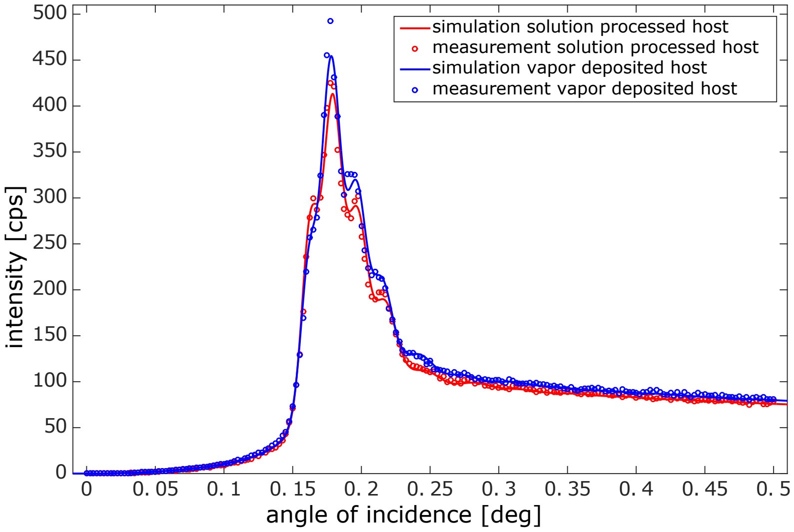

Figure 5.25: S-Kα GIXRF curve of layer stack samples (buffer 20 nm/HTL 20 nm/host 60 nm) with differently prepared host layers.

between the layers was proposed by researchers in reference [23]. This concept was integrated in the theoretical sample description to set up a fitting model for JGIXA. Therefore a model with an interlayer and one without have been tested. However, the best agreement between calculated and measured data was obtained without an interface layer. The formation of an interface layer could not be observed for the

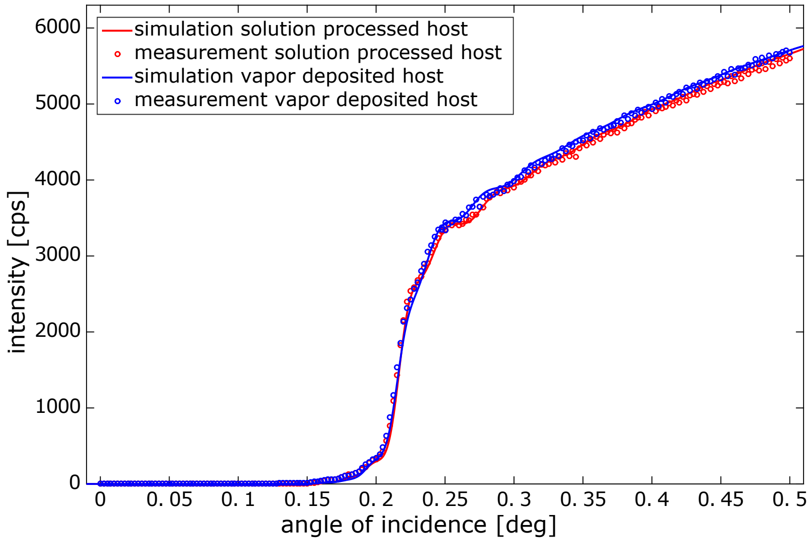

Figure 5.26: Si-Kα GIXRF curve of layer stack samples (buffer 20 nm/HTL 20 nm/host 60 nm) with differently prepared host layers.

solution processed sample.

The results of the calculated values for the model with the best agreement between calculated and measured angle curves are shown in tables 5.5 and 5.6. As for the single layer samples, calculated thickness values are in good agreement with the given values from manufacturing, which were 20 nm for buffer and HTL and 60 nm for the host layer. The calculated thickness of the vapor deposited host is 4 nm above the proposed value of 60 nm, while it is only 56 nm for the solution processed host. This lower thickness for the solution processed host in comparison to the vapor deposited one is on one hand in accordance to the results of the single layer samples and on the other hand also similar to results of the TEM-EDX measurement of similar samples. The higher roughness of the vapor deposited host layer compared to the solution processed host and the similar density values correspond to the single layer results.

Due to the lack of a thin film standard sample with known S concentration, the S content for the vapor deposited sample was set to 1.3 %. This value represents the nominal S concentration based on the chemical composition of the host molecule. It was used as a reference point for subsequent calculations on other, e.g., solution processed samples. Therefore the calculated S concentrations from the other samples or layers are relative to it. The layers below the vapor deposited host, show no significant S concentration for the best model.

The calculated S concentration in the solution processed host layer is quite similar to the expected value. The layers beneath the solution processed host layer show both a significant S content, which is clearly not present in the layers beneath the vapor deposited host. This result is in good agreement to the TEM-EDX measurements, described in the section before.

Table 5.5: Results of the vapor deposited host multilayer sample

Layer	Thickness (nm)	Density (g/cm^3)	Roughness (nm)	S concentration (at%)
H_2O	1.02	0.47	0.88	
Host	64.03	1.22	2.11	1.3 (fixed)
HTL	19.41	0.92	0.95	< 0.002
Buffer	22.69	1.24	1.66	< 0.001

Table 5.6: Results of the solution processed host multilayer sample

Layer	Thickness (nm)	Density (g/cm^3)	Roughness (nm)	S concentration (at%)
H_2O	0.22	0.21	0.42	
Host	55.78	1.21	0.92	1.27
HTL	22.87	1.0	1.56	0.18
Buffer	23.94	1.19	1.57	0.27

5.3 Small Molecule Host Isomer

Both the TEM-EDX and the GIXRF/XRR measurements showed a significant S content in the HTL for the solution processed host layer only. The samples used for both measurements did have a similar architecture. A new sample set should provide samples with equal layer sequence and layer thicknesses. Both TEM-EDX and GIXRF can only describe the distribution of elements but deliver no information on the bond structures. Therefore additional XPS measurements were planned. As XPS is a very surface sensitive method it was necessary to fabricate samples with no Al contact, no ETL and a thinner host layer to facilitate depth profiles.

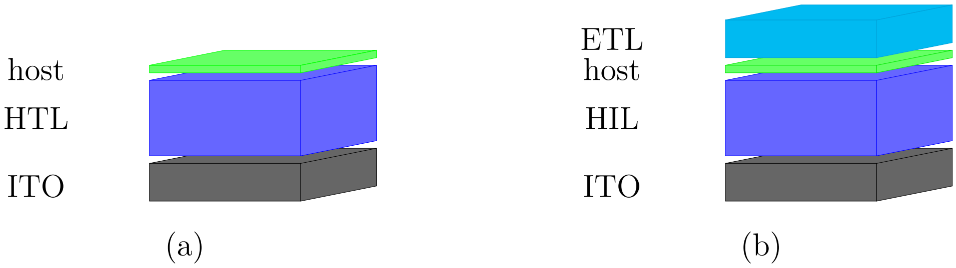

(a) (b)

Figure 5.27: Schematic device architecture of samples for (a) XPS and (b) TEM-EDX with additional ETL and Al.

For these samples an isomer of the original SM host (section 5.2) was used. To compare the behavior of the isomer to the formerly used SM molecule, also TEM-EDX measurement were performed for these samples. Additionally samples for combined GIXRF/XRR measurements were fabricated, as especially the sensitivity of GIXRF for the S content in the HTL can benefit from a thinner host layer. The device structure used is shown in figure 5.27. For XPS measurements the layer sequence was 50 nm ITO/100 nm HTM/10 nm host (figure 5.27a). The samples for the TEM-EDX measurements additionally had 10 nm ETM, 40 nm ETM + Liq and 100 nm Al, as shown in figure 5.27.

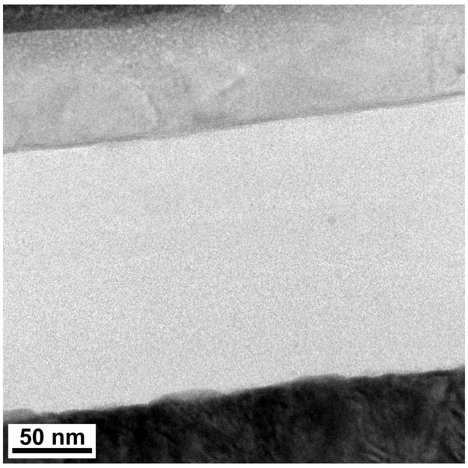

Figure 5.28: TEM-image of a lamella from the SM isomer samples.

Beside the use of an isomer of the SM material, all other materials were kept the same. Also the same preparation conditions were used and the host layers again were either vapor deposited or solution processed.

As for the SM, in the TEM images of the lamella's tip no discrimination within the organic layers is visible. The thickness of the organic layer stack is according to the desired value of 160 nm (figure 5.28). For the BF images in STEM mode, which were used to determine the measurement areas, the S containing layer was also invisible.

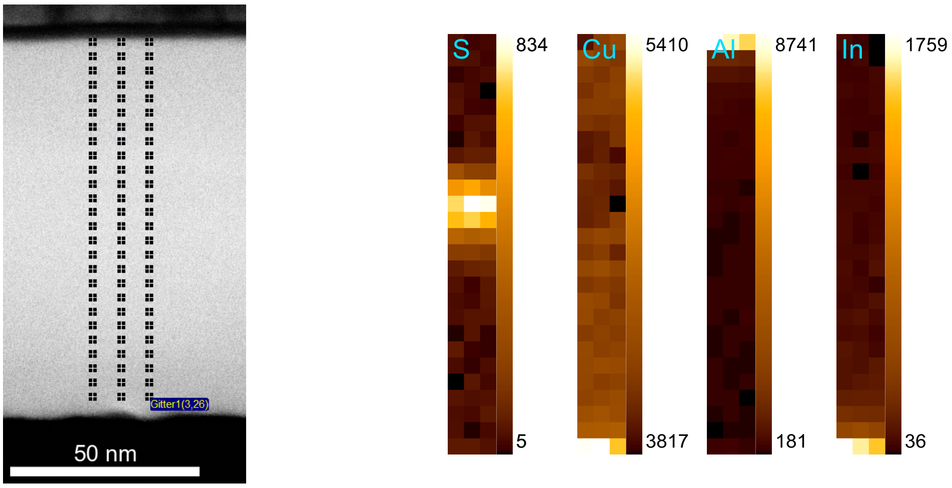

Figure 5.29: Left: BF image of the investigated area with grid of measurement points, right: element maps for selected elements of a sample with vapor deposited host layer.

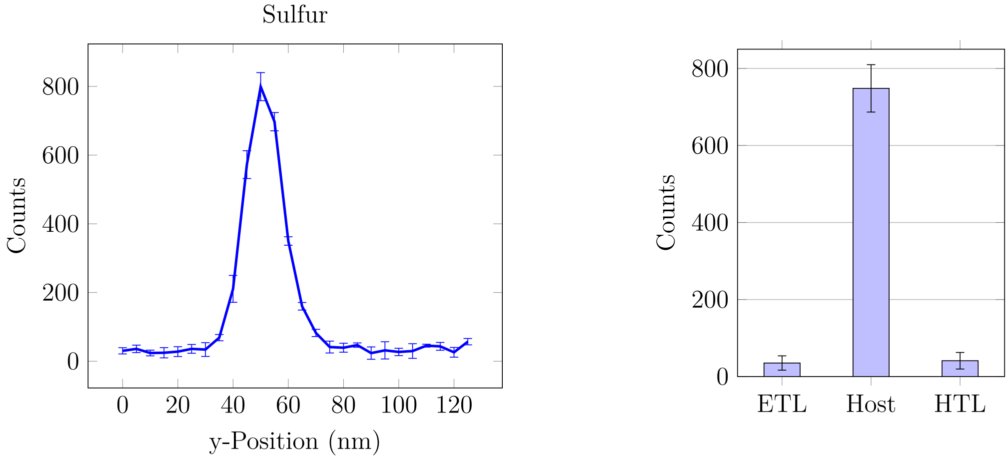

Figure 5.30: Left: averaged S distribution along the cross section (y=0 corresponds to the Al contact, y=125 to the ITO contact), right: averaged S counts from the segmented area scan of a sample with vapor deposited host layer.

The samples with vapor deposited host layer showed no significant S counts outside of the host layer. For one area scan the BF image and the corresponding element maps for particular elements are displayed in figure 5.29. The S distribution along the cross section is also visualized as line plot in figure 5.30. Again the S net counts were averaged for each line of the area scan. On the right side of this figure additionally the averaged S net counts for the different layers, which were calculated from the segmented area scan, are shown.

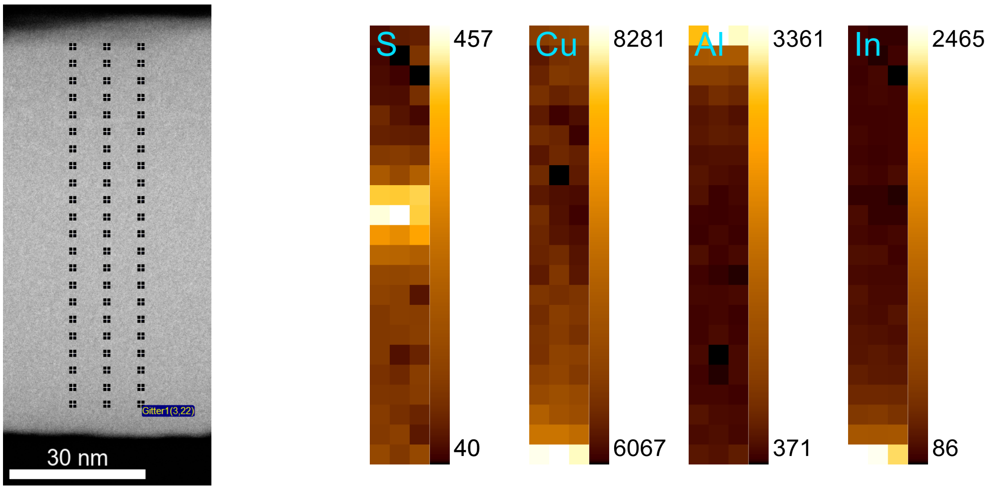

Figure 5.31: Left: BF image of the investigated area with grid of measurement points, right: element maps for selected elements of a sample with solution processed host layer.

As for the SM host samples, a significant S content is detectable in the HTL only beneath the solution processed host layer. The difference between S counts in HTL for differently prepared samples, is smaller than for the previously investigated samples. These deviation is possibly due to the lower thickness of the host layer and therefore less host material. The results of a representative measurement of a sample with solution processed host layer are shown in figures 5.31 and 5.32.

A comparison of results for differently prepared samples is shown in figure 5.33. The S net counts were again normalized to the average count in the host layer in order to make the measurements from different lamellas comparable.

The result for the SM isomer is similar to those of the original SM host material. There is a significant S count within the HTL for the samples with solution processed host layer. The effect is less prominent as the host layer is only 10 nm thick. The

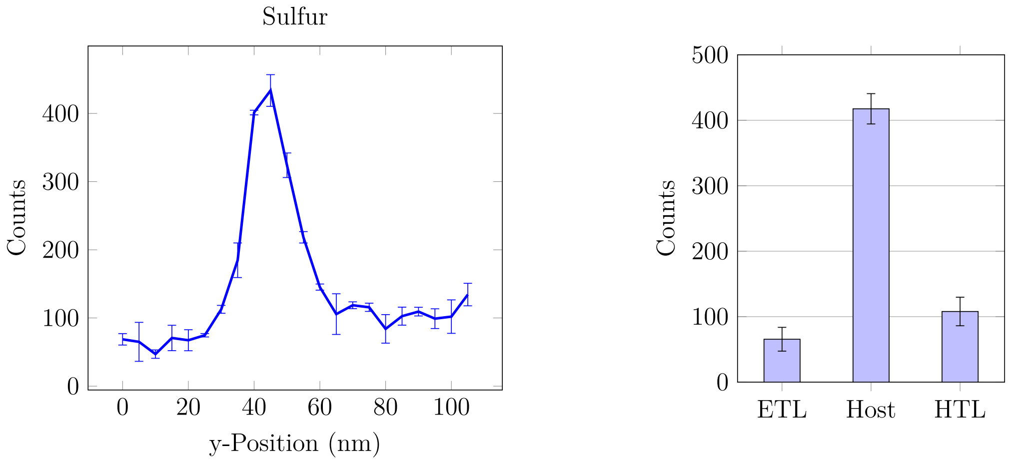

Figure 5.32: Left: averaged S distribution along the cross section (y=0 corresponds to the Al contact, y=105 to the ITO contact), right: averaged S counts from the segmented area scan of a sample with solution processed host layer.

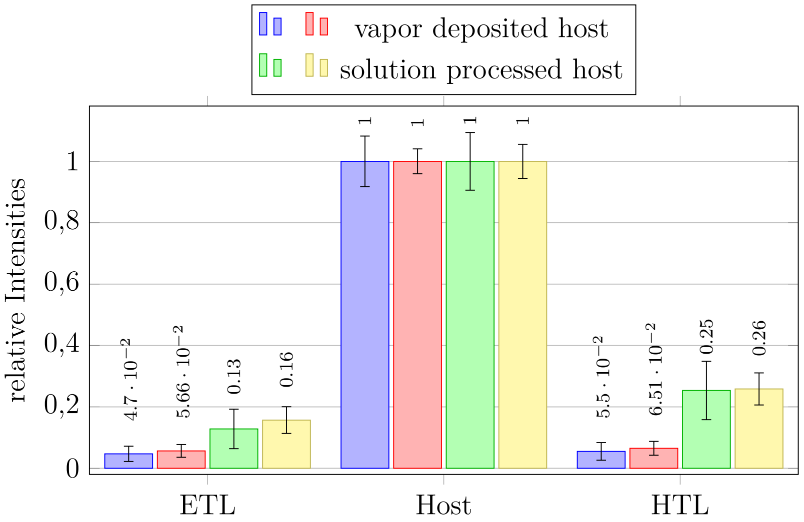

Figure 5.33: Comparison of normalized S net counts within the organic layers of samples with differently prepared host layer, derived from fragmented area scans.

width of the S peak, which depicts the host layer thickness, is not reduced for the samples with solution processed host. This is shown in figure 5.34, which compares the S distribution along the cross section for four different measurements. The fact that the solution processed host layer thickness appears not reduced, may also be an

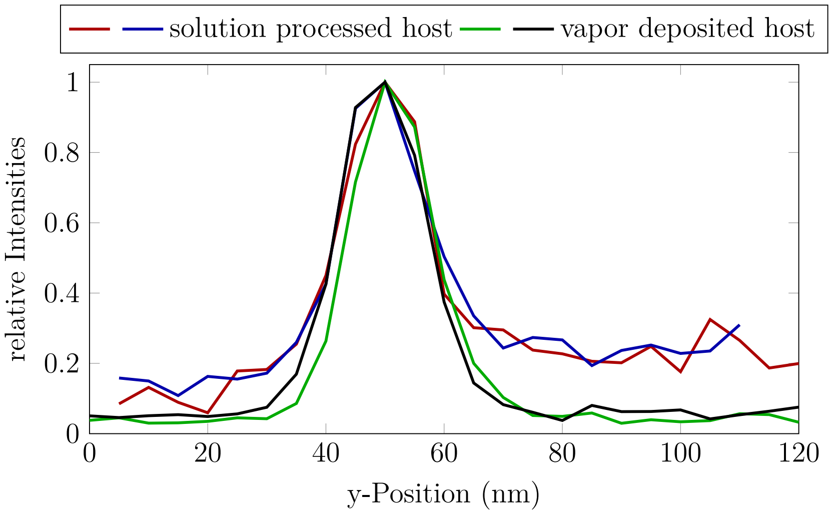

Figure 5.34: Comparison of the normalized S distribution along the sample's cross section from different 10 nm×10 nm area scans of samples with differently prepared host layer.

effect of the smaller thickness of the host layer. Noticeable are the higher S net counts in the ETL of the sample with solution processed host layer, while in the samples with vapor deposited host layer no significant S count could be detected. This may be an effect caused by the normalization process. When the averaged net count for S is lower in the solution processed host layer, for example due to a lower S concentration, the S counts in the other layers would be overestimated. This has no influence on the general result that only for the solution processed host samples a significant S count can be found in the HTL.

5.3.1 Grazing Incidence X-ray Fluorescence and X-ray Reflectometry

The samples for combined GIXRF/XRR measurements were fabricated on SiO_2 substrates. The 10 nm thick host layer was either vapor deposited or solution processed onto a 100 nm thick solution processed and annealed HTL. The schematic architecture is equal to the XPS samples, shown in figure 5.28a but without the ITO layer underneath the HTL. In comparison to the first layer stacks which were investigated with GIXRF/XRR with a 60 nm thick host layer, the thickness of 10 nm is closer to a real device. Additionally, self absorption of the S signal will be higher in a host layer with a thickness of 60 nm.

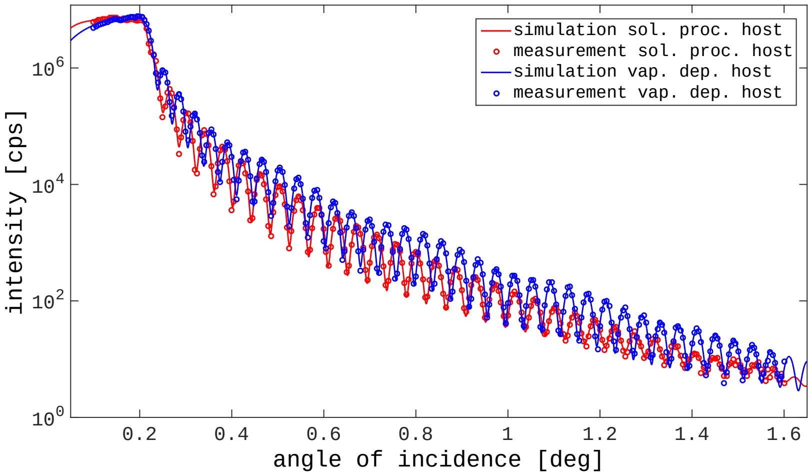

Figure 5.35: XRR curve of layer stack samples (HTL 100 nm/host 10 nm) with differently prepared host layers.

The XRR angle curves for samples with differently prepared host layer in figure 5.35 show clear differences. While oscillation width is quite similar, indicating comparable film thicknesses, the curve for the solution processed host layer declines faster. In general the intensity of the reflected beam decreases faster with increasing surface roughness. Interface roughness influences the amplitude of the oscillation, together with the density difference between the layers. As for the SM molecule host samples in section 5.2.1, the oscillation of the reflectivity curve is relatively even. The sample with the vapor deposited host layer shows a more uneven pattern, but more even compared to the reflectivity of the vapor deposited sample with the SM molecule host.

A comparison of two S-Kα signals, one from a vapor deposited host layer, one from a solution processed host, is shown in figure 5.36. While the samples with the 60 nm host showed rather small variations between differently prepared samples, the S-Kα GIXRF curves of the SM isomer samples with 10 nm host show clear differences in shape for differently prepared samples. The shape of the S curve for the solution processed host layer resembles the curve obtained from the 60 nm host samples. The curve from the sample with vapor deposited host layer shows a distinctly different shape: The signal

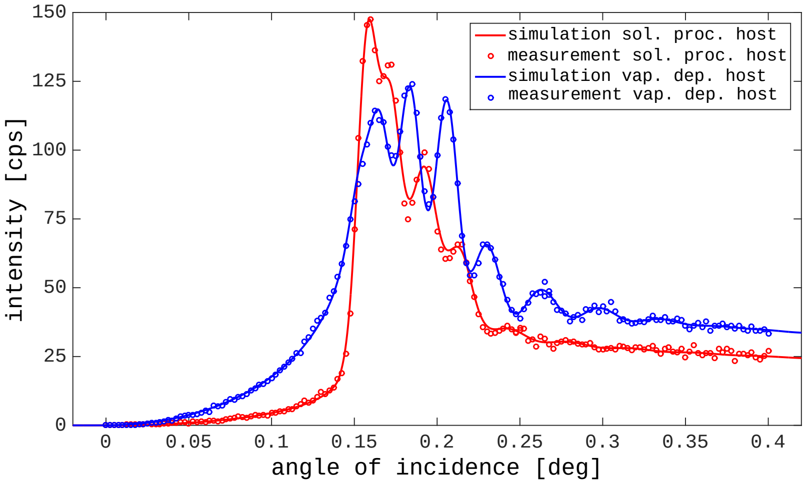

Figure 5.36: S-Kα GIXRF curve of layer stack samples (HTL 100 nm/host 10 nm) with differently prepared host layers.

increases much earlier but with a more shallow climb. The maximum count rate is lower and on the second peak instead of the first.

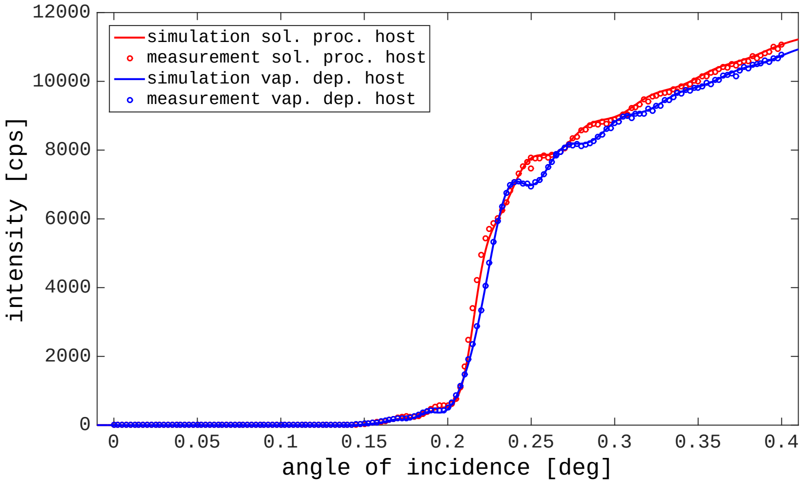

Figure 5.37: Si-Kα GIXRF curve of layer stack samples (HTL 100 nm/host 10 nm) with differently prepared host layers.

Also the Si-Kα GIXRF curve shows different features for the differently prepared

Table 5.7: Results of the vapor deposited host multilayer sample

Layer	Thickness (nm)	Density (g/cm^3)	Roughness (nm)	S concentration (at%)
H_2O	0.31	0.68	0.49	
Host	13.24	1.28	1.48	0.95
HTL	96.56	0.99	1.16	< 0.009

Table 5.8: Results of the solution processed host multilayer sample

Layer	Thickness (nm)	Density (g/cm^3)	Roughness (nm)	S concentration (at%)
H_2O	0.02	0.54	0.42	
Host	11.17	1.06	1.13	0.20
HTL	89.8	1.01	0.004	0.08

samples (figure 5.37). The overall shape of the Si-Kα curve is typical for the signal from bulk material. Fluctuations, which could be seen before and after the steep intensity increase, are caused by the interaction of the reflected signal with the layers above the substrate.

The results of sample modeling with JGIXA are shown in tables 5.7 and 5.8. In general, calculated thickness values are in good agreement to the estimated value of 10 nm for the host layer and 100 nm for the HTL. However, for the vapor deposited host and HTL, measured thickness values tend to be slightly higher than for the sample with solution processed host layer.

For the quantification of the S amount external standards were used. One was a known titanium (Ti) layer on an Si wafer, the other one a mixture of Ti and S liquid standard material applied on a quartz substrate. For these samples the concentrations are known and therefore the relative sensitivity of S to Si could be calculated. The advantage of this method is the independence of special layer standards for the specific samples investigated. For the samples used the quantification of the S concentration with this method yields a distinctively smaller value than estimated from the amount of S in the molecule, which would be 1.3 %. Especially the S value for the sample with solution processed host layer is with 0.2 % well below the expectation. Despite this

Table 5.9: Results of the solution processed host multilayer sample modeled with an intermixing layer between host and HTL

Layer	Thickness (nm)	Density (g/cm^3)	Roughness (nm)	S concentration (at%)
H_2O	0.11	0.71	0.53	
Host	10.20	1.08	1.42	0.2
intermixing	31.16	1.06	2.29	0.1
HTL	59.61	1.02	3.00	0.08

discrepancy in the S concentration value, the observation that a significant S amount in the HTL could only be found in the layer beneath the solution processed host layer is still valid. The calculated S concentration in the HTL beneath the solution processed layer is more than 10 times higher than the concentration beneath the vapor deposited host layer.

The calculated interface roughness of the HTL layer seems to be very low with a value of 0.004 nm. This can be an indication that the assumed model is not correct for this sample. Therefore, the possibility of the formation of an intermixing layer between solution processed host layer and HTL has been integrated into a sample model for fitting the acquired angle curves. The results of the model with an intermixing layer are shown in table 5.9. With an extra interface layer in the model the resulting interface roughness is more consistent with the other roughness values. The thicknesses of the interface layer and the HTL add up to 90.77 nm, which is comparable to the thickness of the HTL layer in the model without intermixing layer. Intermixing layer and HTL show a significant S concentration.

5.3.2 X-ray Photoelectron Spectroscopy

To investigate the S content in the HTL further, XPS measurements were performed. To measure the HTL the 10 nm host layer had to be removed with the sputter gun. Sputter conditions as energy of Ar clusters, sputter duration or necessary number of etch cycles were determined for samples with solution processed host layer and those with vapor deposited host. For comparison the procedure of the depth profile was the same for both samples sets. Final measurements were performed on till then unused samples.

For better visibility not all spectra from one depth profile are plotted. After the first spectrum, which corresponds to the sample surface before etching, only every other spectrum is plotted. In the survey spectrum for both sample sets beside S, C, nitrogen (N) and oxygen (O) could be found. Both in the SM host and in the HTL polymer no O is present within the molecule.

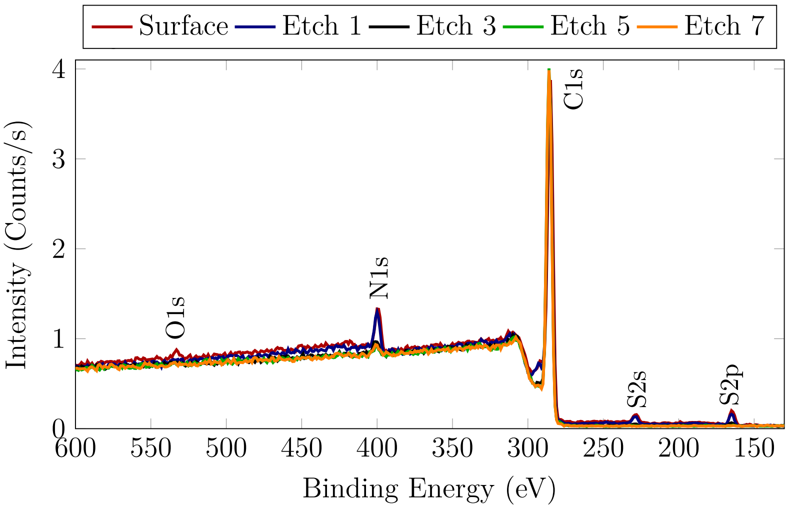

Figure 5.38: Selected survey spectra from the depth profile of a SM isomer sample with vapor deposited host layer with labeled peaks.

Selected survey spectra for the sample with vapor deposited host layer are shown in figure 5.38. Only on the surface O is present, pointing to surface contamination, as the samples were transported to the XPS through ambient atmosphere. The O signal vanishes after the first etch. The N signal suddenly decreases before etch 4, but stays stable afterwards.

The S2p scan for the sample with vapor deposited host in figure 5.39 shows that almost no S can be detected after etch 5. Therefore a reasonable assumption is that the host layer was fully removed, since no significant S content was found in the HTL by TEM-EDX analysis.

In the survey spectra for the sample with solution processed host layer in figure 5.40, the comparatively high and consistent O signal is striking. The N signal does not change with depth for this sample.

For the S2p scans in figure 5.41 even after etch 9 a S signal is still visible. This matches the TEM-EDX results that S is detectable through the HTL for the sample

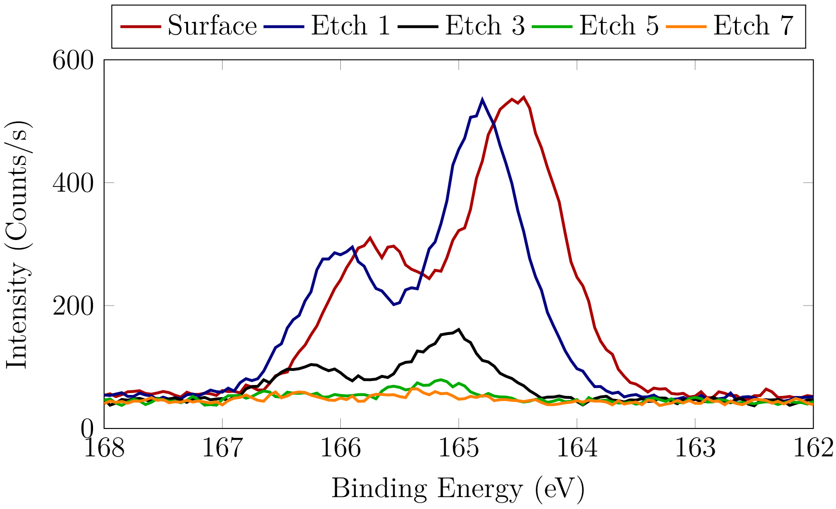

Figure 5.39: Selected S2p spectra from the depth profile for the SM isomer sample with vapor deposited host layer.

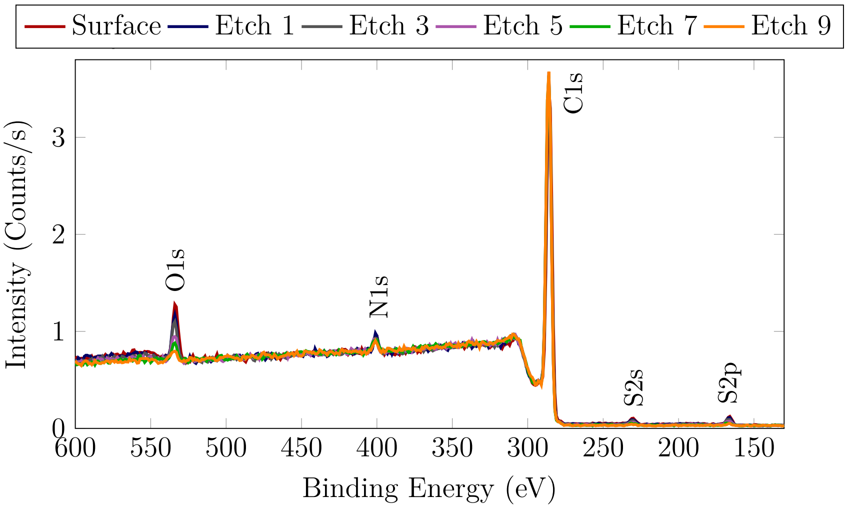

Figure 5.40: Selected survey spectra from the depth profile of a SM isomer sample with solution processed host layer with labeled peaks.

with solution processed host layer only.

The S2p scans of both samples show a shift to higher binding energies between the measurement from the surface and the one after the first etch. The peaks afterwards only shift relatively little compared to the first shift. The first shift may be caused by differences between the host material on the surface, which was exposed to ambient atmosphere, and the unaltered host layer beneath the surface. The slight shift

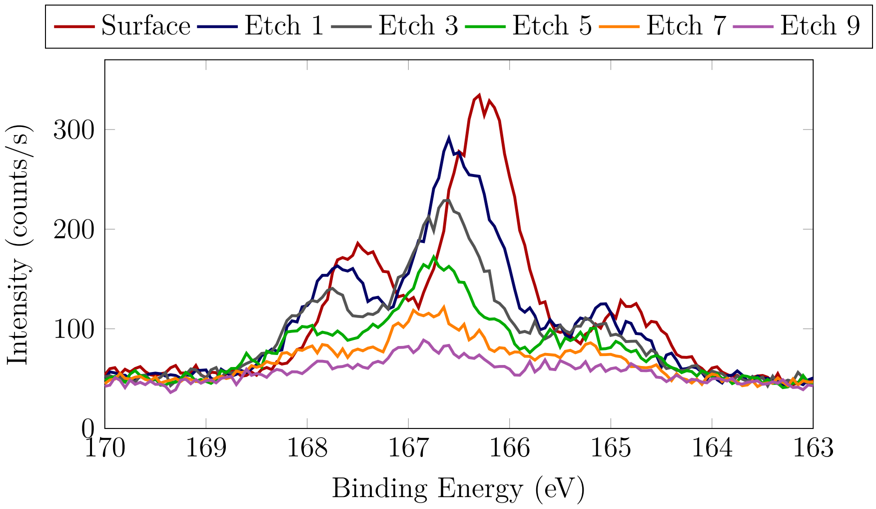

Figure 5.41: Selected S2p spectra from the depth profile for the SM isomer sample with solution processed host layer.

afterwards may be caused by charge effects, as the sample materials are not good conductors. As the shape of the S peaks does not change beside of the slight energy shift, it is reasonable to assume that the whole SM diffuses to the HTL, when the host layer is solution processed.

5.4 Polymer Material

In comparison to the SM host material a S based polymer material was also investigated to see if a similar effect of a significant S count in the layer beneath a solution processed EML can be detected.

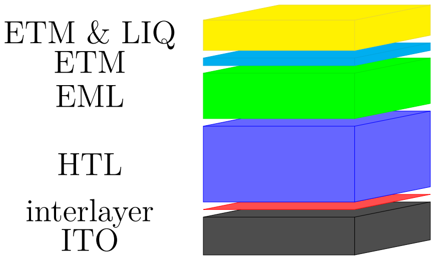

Figure 5.42: Schematic device architecture of samples with solution processed polymer EML.

The devices had the following structure: 50 nm ITO/100 nm HTL/60 nm EML/

10 nm ETM/40 nm ETM + Liq/100 nm Al. A schematic of the device structure is shown in figure 5.42.

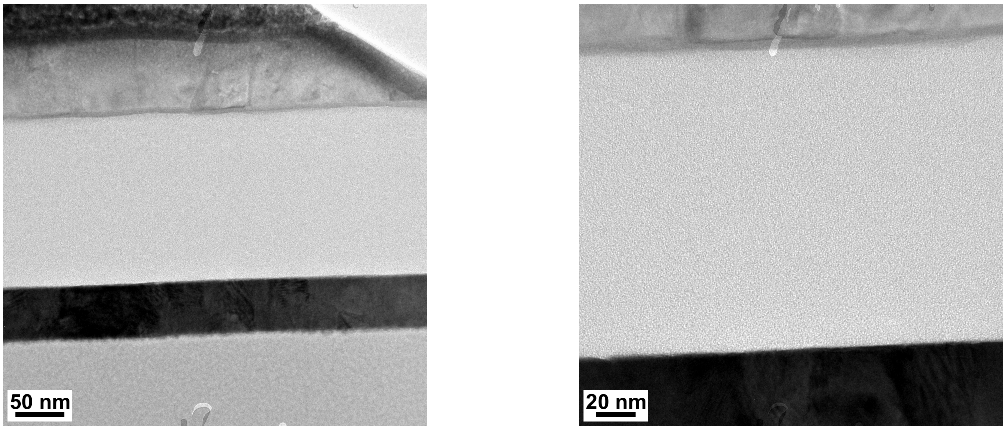

Figure 5.43: TEM images of the organic layer stack of samples with solution processed polymer EML.

The materials used for HTL and ETL remain unchanged from the SM samples. They were also processed in the same way. The EML consists of a copolymer with a molecular weight of 470 000 g/mol, which satisfies the task of a host as well as the one of an emitter in one molecule. The polymer chain is made of alternating units of substituted spiro units and benzothiadiazol units. Alkylene groups attached to the spiro units improve solubility. The benzothiadiazol units contain S in this material. Layers from this polymer were spin coated from a 13 mg/mL toluene solution and subsequently annealed for 10 min at 180 °C in a nitrogen glove box.

As with the other sample sets discussed previously, two lamellas were prepared following the routine, described in chapter 4.2. The TEM images did not reveal the layered structure in the organic layers, but the electrodes are clearly identifiable, as can be seen in figure 5.43. The BF image of one area scan and the corresponding element maps are shown in figure 5.44. The averaged S counts along the cross section and a comparison of net counts in the different layers can be seen in figure 5.45. The EDX measurements reveal the maximum S count within the EML. Neither electron transport material (ETM) nor HTM contain S. The results of the first two lamellas were both revealing a significant S net count in the HTL. The HTL layer also showed a clearly higher S count than the ETL.

The layered structure of the sample is again visualized in figure 5.49a, by overlapping the normalized line plots of selected elements. As the measurement area was

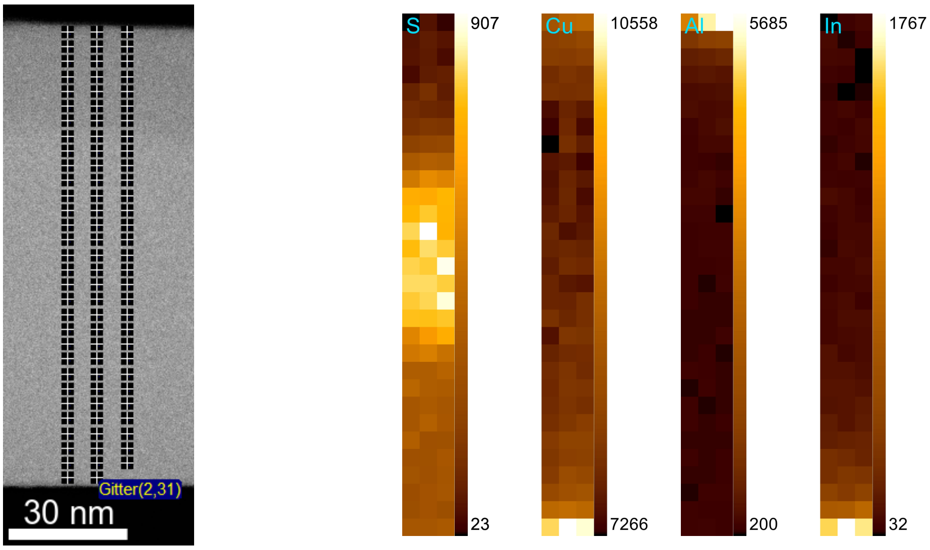

Figure 5.44: Left: BF image of the investigated area with grid of measurement points, right: element maps for selected elements of a sample with solution processed polymer EML.

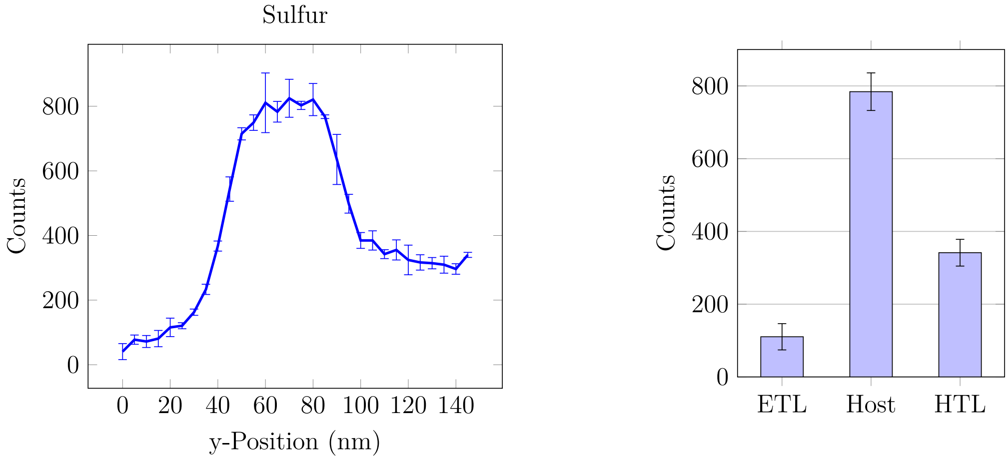

Figure 5.45: Left: averaged S distribution along the cross section (y=0 corresponds to the Al contact, y=145 to the ITO contact), right: averaged S counts from the segmented area scan of a sample with solution processed polymer EML.

chosen to start and end at the edge of the contacts, the variation of the relative intensity of the Cu signal is minimal.

The normalized S counts in the different organic layers were compared to the results

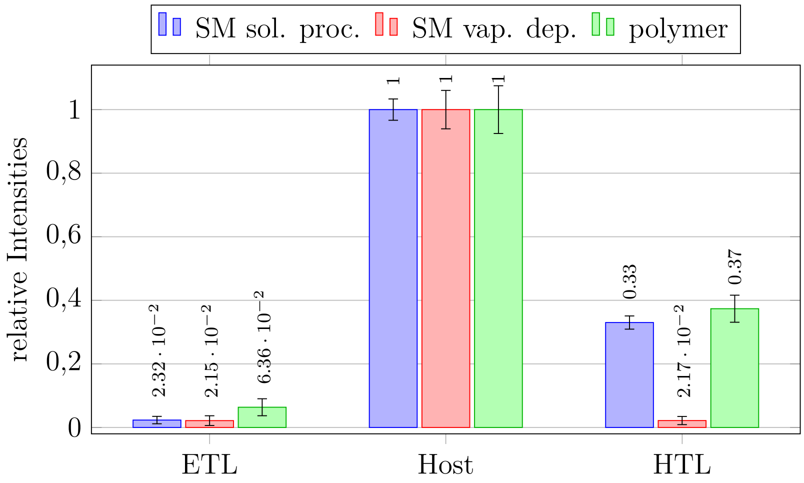

Figure 5.46: Comparison of normalized S net counts within the organic layers of samples with differently prepared host layer, derived from line scans scans.

of the SM host samples (see figure 5.46). For the HTL both samples with polymer EML and solution processed host layer showed a significant amount of S counts. While the S signal in the ETL is nearly the same for both SM samples, it is clearly higher for the polymer sample. This can be an artifact caused by the normalization to the respective maximum S count. A lower S concentration in the polymer EML would lead to a lower S signal. The S concentration in the EML, calculated from the chemical formula, is slightly lower for the polymer material than for the SM host. Therefore the normalization to the maximum S count, would mean that a comparable S count in the ETL would lead to a higher fraction for an EML with lower S concentration, when compared to an EML with higher S concentration. But as the S count for the HTL is two orders of magnitude higher than the one in the ETL, the conclusion that some of the S is transferred from the EML still holds. However, in order to verify this result an additional lamella was fabricated from the same pixel as the two lamellas before, but from a different location within the pixel.

Results of the third lamella are shown in figures 5.47 and 5.45. The S distribution along the sample's cross section reveals the 60 nm thick EML. For the HTL the S signal is clearly lower than for the measurements of the other two lamellas from the same sample type. The relatively high S count in the ETL is also detected in the third sample.

A comparison between the results of the three lamellas is shown in figures 5.50 and

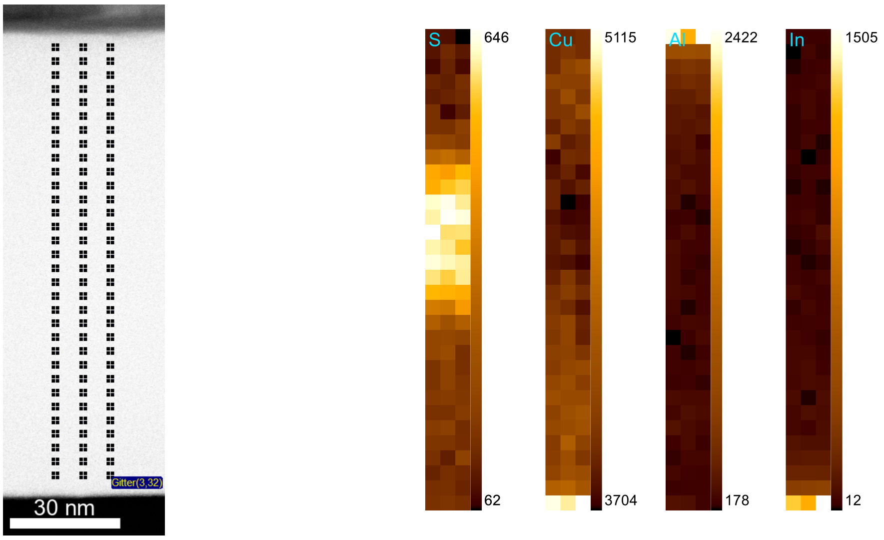

Figure 5.47: Left: BF image of the investigated area with grid of measurement points, right: element maps for selected elements of a sample with solution processed polymer EML.

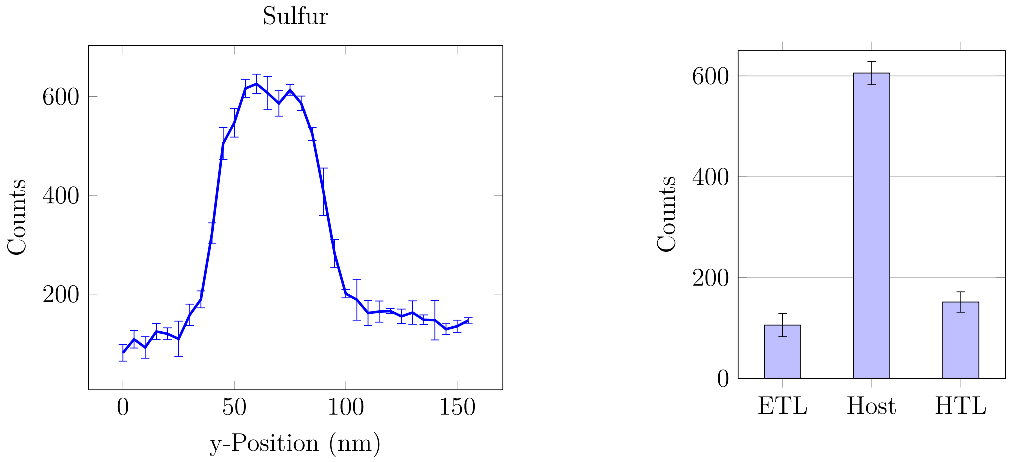

Figure 5.48: Left: averaged S distribution along the cross section (y=0 corresponds to the Al contact, y=155 to the ITO contact), right: averaged S counts from the segmented area scan of a sample with solution processed polymer EML.

5.51. The normalized S distribution along the sample's cross section is very similar for all three area scans. A noticeable difference arises in the HTL region. While for two lamellas a clearly elevated S signal is detected, the third lamella shows a

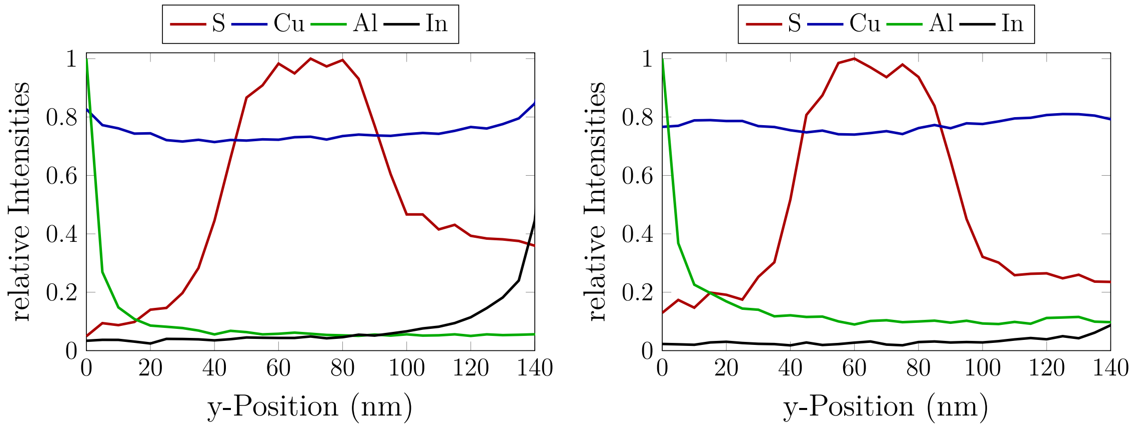

(a)

(b)

Figure 5.49: Normalized line plots for the elements S, Cu, Al, and In along the cross section of two samples with solution processed polymer EML.

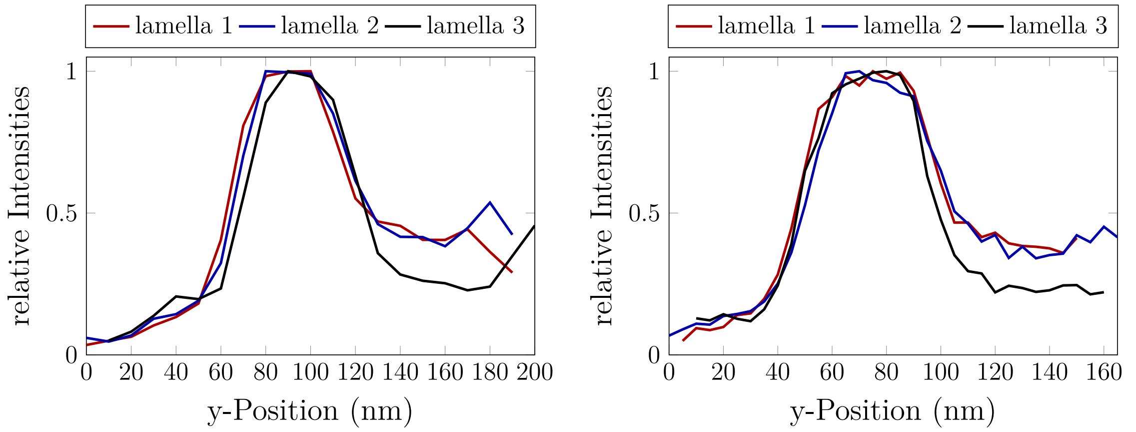

(a)

(b)

Figure 5.50: Comparison of the normalized average S distribution along the sample's cross section from different (a) 10 nm×10 nm and (b) 10 nm×5 nm area scans of samples with solution processed polymer EML.

significantly lower S net count. This difference applies for the 10 nm×10 nm as well as for the 10 nm×5 nm scans, in figure 5.50a and b respectively. The comparison of the averaged S counts in the respective layers gives a comparable S portion in the ETL, but the S fraction in the HTL varies. Including the error margin the ratio for S in the HTL for the third lamella is still above the ratio in the ETL.

For this sample type a final result remains somewhat unclear. While the first two

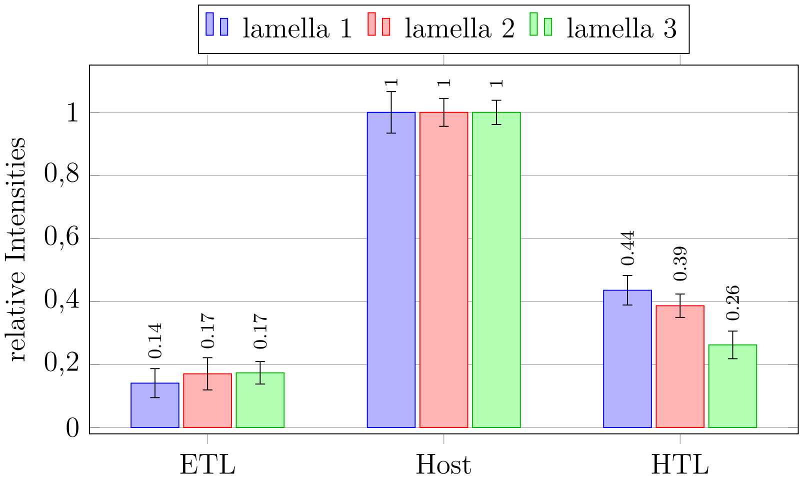

Figure 5.51: Comparison of normalized S net counts within the organic layers of three lamellas from samples with solution processed polymer EML layer, derived from segmented area scans scans.

lamellas showed a clear elevated S content in the HTL, this could not be shown for a lamella from another area of the pixel. As there was some S detectable within the HTL, the cross linking of the HTL seems not strong enough to withstand the contact with the solvent while preparation of the host layer.

The TEM-EDX measurements cover only a very small area compared to the size of the hole pixel. A lamella is about 10 nm long and even on the thick end of the wedge shape about 700 nm thick, while the pixel area is 2 mm×2 mm. Therefore it is necessary to assume a homogeneous sample composition, for a lamella to be representative. One way to accomplish a complete characterization of this particular sample set would be the preparation of lamellas in a regular grid all over the pixel. As the preparation of TEM is quite time consuming, other means to determine sample homogeneity should be considered first.

6 Conclusions

As stated in the introduction, the main aim of this work was the comparison of differently prepared organic thin film samples. Differences in life time and efficiency have been shown before [21, 22]. Several studies suggest that the packing density is lower for solution processed organic films, which could influence charge carrier transport [20, 80]. In the present work the differences in regard to the spatial distribution of specific elements were investigated. The desired result would be, that regardless of the preparation method no significant differences in the organic layer stacks would be observable. The analysis of differently prepared thin film samples shows that this is not the case. Here the differences in the layered structure depending on preparation method were observed. The element S, which is part of the SM host material, could be found in the HTL beneath the host layer only if the host was solution processed. No S could be found in the HTL if the host was vapor deposited. As S is not part of the HTL material used, it is reasonable to assume a displacement of S during production of the layered structure. One possible explanation of the dislocated S is, that when applying the host layer using a solution, the underlying layer is at least partially dissolved, allowing the S to relocate into the HTL [38, 81]. A possible S residue originating from the solvent used, could be ruled out by investigating a control sample consisting only of a solution processed HTL. As diffusion processes are temperature dependent, annealing the layer stack after solution processing the host layer could faciliate the SM hosts dispersal [82, 83].

Annealing of the HTL cross links the materials side chains and should render the layer insoluble. For the investigated samples with solution processed host layer, the HTL seems to have been insufficiently protected against the solvent, while applying the host layer. A possible solution might be the use of a different solvent for the application of the host layer [84]. Another could be better stabilization of the HTL.

If the whole SM diffuses, a reasonable assumption is that S remains bound to the same molecule. The binding state was analyzed using XPS. Depth profiling was used to determine the S binding state across the interface of host and HTM. Changes in the binding state of S would manifest themselves by shifted peaks. No such peak shift could be observed, apart from a minor change at the sample surface. It is therefore reasonable to deduce, that no change in the binding state has occurred and the whole molecule diffused into the HTL. According to the TEM-EDX measurements S can be found in the whole 100 nm thick HTL. The S distribution appears uniformly, no depth dependent gradient could be detected. This indicates that not only the surface of the HTL is affected by the preparation of the solution processed host layer, but the whole HTL.

As stated above differences in efficiency and life time can be observed, when solution processed OLEDs are compared to vapor deposited ones [21, 38]. Often this disparity arises as result of different device architecture. For vapor deposited OLEDs it is manageable to fabricate multilayer devices where every layer serves a specific task. Solution processed OLEDs often have only two or three layers. But even for devices with the same architecture, differences in performance and life time occur [20, 22, 85]. The performance of an OLED is highly dependent on an unhindered transport of the injected charge carriers and their preferably complete recombination in the EML. If the whole SM host molecule migrates into the HTL, these molecules can disturb the hole transportation in the HTL. Therefore the SM could have an influence on efficiency and also lead to effects similar to impurity-induced degradation [86]. For the further improvement of solution processed OLEDs the prevention of layer intermixing is imperative.

The change in S distribution for differently prepared samples was observed using TEM-EDX and GIXRF/XRR. The preparation of TEM lamellas facilitated direct access to the cross section of the organic layer stack for investigation in a TEM. As the different organic layers show very little contrast difference in TEM images, spatially resolved elemental analysis provided information about specific layers in the stack. TEM-EDX utilizes the high resolution in the low nm range achievable in a TEM.

For GIXRF/XRR measurements no special sample preparation is necessary. Any influence of the sample preparation by FIB milling can therefore be excluded. The layered structure is analyzed indirectly, providing information on layer thickness, surface or interface roughness and elemental distribution.

Apart from the results regarding differently prepared layer stacks, it could also be shown that a combined GIXRF/XRR analysis can be a valuable tool for the investigation of organic thin films. Despite the very small variations in electron density of the different layers and only one element which could be analyzed using its characteristic X-rays in air using an energy dispersive system, data with sufficient quality for fitting could be acquired.

This complimentary method not only validated the TEM-EDX results, it can also be a powerful tool on its own. Sample preparation is minimal compared to FIB milling which is required for TEM analysis. Existing X-ray diffractometers can be used for GIXRF/XRR analysis with only a few changes necessary, in particular the addition of an energy dispersive detector. Specialized equipment might improve performance even further, e.g. analyzing under vacuum condition. However, no dedicated GIXRF/XRR spectrometer is currently commercially available.

One main difference between TEM-EDX and GIXRF/XRR is the inspected area. TEM lamellas were prepared from 2 mm×2 mm pixels and were about 15 µm long with a thickness of less than 100 nm at the tip and about 300 nm in the region the EDX scans were performed. A homogenous sample is necessary for the lamella being representative for the sample. The inspected area in GIXRF/XRR is in the order of several mm^2, up to cm^2. Depending on the sample it can be advantageous to gain information of a particular spot or averaging over a larger area.

A possible drawback of GIXRF/XRR is the challenging data analysis. Dedicated software packages are available [58, 76], but a suitable model has to be supposed to analyze the data, which might lead to some ambiguity and also requires substantial knowledge about the sample.

Bibliography

[1] O. Nuyken, S. Jungermann, V. Wiederhirn, E. Bacher, and K. Meerholz: *Modern Trends in Organic Light-Emitting Devices (OLEDs).* Monatsh. Chem., 137:811–824, 2006. doi 10.1007/s00706-006-0490-4.

[2] B. Geffroy, P. le Roy, and C. Prat: *Organic light-emitting diode (OLED) technology: materials, devices and display technologies.* Polym. Int., 55:572–582, 2006. doi 10.1002/pi.1974.

[3] S. Lee, J. H. Kwon, S. Kwon, and K. C. Choi: *A Review of Flexible OLEDs Toward Highly Durable Unusual Displays.* IEEE Trans. Electron Devices, 64:1922–1931, 2017. doi 10.1109/TED.2017.2647964.

[4] F. So, J. Kido, and P. Burrows: *Organic light-emitting devices for solid-state lighting.* MRS Bulletin, 33:663–669, 2008. doi 10.1557/mrs2008.137.

[5] Y. S. Tyan: *Organic light-emitting-diode lighting overview.* J. Photon. Energy, 1:011009–011009–15, 2011. doi 10.1117/1.3529412.

[6] N. Thejo Kalyani and S. J. Dhoble: *Organic light emitting diodes: Energy saving lighting technology - A review.* Renew. Sust. Energ. Rev., 16:2696–2723, 2012. doi 10.1016/j.rser.2012.02.021.

[7] R. P. Xu, Y. Q. Li, and J. X. Tang: *Recent advances in flexible organic light-emitting diodes.* J. Mater. Chem. C, 4:9116–9142, 2016. doi 10.1039/C6TC03230C.

[8] G. Gu, V. Bulović, P. E. Burrows, S. R. Forrest, and M. E. Thompson: *Transparent organic light-emitting devices.* Appl. Phys. Lett., 68:2606–2608, 1996. doi 10.1063/1.116196.

[9] J. H. Chang, W. H. Lin, P. C. Wang, J. I Taur, T. A. Ku, W. T. Chen, S. J. Yan, and C. I Wu: *Solution-processed transparent blue organic light-emitting diodes with graphene as the top cathode.* Sci. Rep., 5:9693, 2015. doi 10.1038/srep09693.

[10] S. Pang, X. Hernandez, Y.and Feng, and K. Müllen: *Graphene as Transparent Electrode Material for Organic Electronics.* Adv. Mater., 23:2779–2795, 2011. doi 10.1002/adma.201100304.

[11] T. Tsujimura: *Organic Light-Emitting Diodes (OLEDs).* Wiley, Hoboken, 2017, ISBN 9781119187318.

[12] A. Köhler and H. Bässler: *Electronic Processes in Organic Semiconductors.* Wiley-VCH, Weinheim, 2015, ISBN 9783527332922.

[13] A. Bernanose, M. Comte, and P. Vouaux: *A new method of emission of light by certain organic compounds.* J. Chim. Phys., 50:64, 1953.

[14] M. Pope, H. P. Kallmann, and P. Magnante: *Electroluminescence in Organic Crystals.* J. Chem. Phys., 38:2042–2043, 1963. doi 10.1063/1.1733929.

[15] C. W. Tang and S. A. Van Slyke: *Organic electroluminescent diodes.* Appl. Phys. Lett., 51:913–915, 1987. doi 10.1063/1.98799.

[16] J. H. Burroughes, D. D. C. Bradley, A. R. Brown, R. N. Marks, K. Mackay, R. H. Friend, P. L. Burns, and A. B. Holmes: *Light-emitting diodes based on conjugated polymers.* Nature, 341:539–541, 1990. doi 10.1038/347539a0.

[17] A. Buckley: *Organic Light-Emitting Diodes (OLEDs).* Woodhead Publishing, Cambridge, 2013, ISBN 9780857094254.

[18] K. Müllen and U. Scherf: *Organic Light Emitting Devices: Synthesis, Properties and Applications.* Wiley-VCH, Weinheim, 2006, ISBN 9783527312184.

[19] M. A. Baldo, D. F. O'Brien, Y. You, A. Shoustikov, S. Sibley, M. E. Thompson, and S. R. Forrest: *Highly efficient phosphorescent emission from organic electroluminescent devices.* Nature, 395:151–154, 1998. doi 10.1038/25954.

[20] T. W. Lee, T. Noh, H. W. Shin, O. Kwon, J. J. Park, B. K. Choi, M. S. Kim, D. W. Shin, and Y. R. Kim: *Characteristics of Solution-Processed*

Small-Molecule Organic Films and Light-Emitting Diodes Compared with their Vacuum-Deposited Counterparts. Adv. Funct. Mater., 19:1625–1630, 2009. doi 10.1002/adfm.200801045.

[21] X. Xing, L. Zhong, L. Zhang, Z. Chen, B. Qu, E. Chen, L. Xiao, and Q. Gong: *Essential Differences of Organic Films at the Molecular Level via Vacuum Deposition and Solution Processes for Organic Light-Emitting Diodes.* J. Phys. Chem. C, 117:25405–25408, 2013. doi 10.1021/jp410547w.

[22] S. Liu, C. Peng, A. Cruz, Y. Chen, and F. So: *Degradation study of organic light-emitting diodes with solution-processed small molecule phosphorescent emitting layers.* J. Mater. Chem. C, 4:8696–8703, 2016. doi 10.1039/C6TC02962K.

[23] V. R. Nikitenko, V. I. Arkhipov, Y. H. Tak, J. Pommerehne, H. Bässler, and H. H. Hörhold: *The overshoot effect in transient electroluminescence from organic bilayer light emitting diodes: Experiment and theory.* J. Appl. Phys., 81:7514–7525, 1997. doi 10.1063/1.365293.

[24] W. Demtröder: *Experimentalphysik 3 - Atome, Moleküle und Festkörper.* Springer, Heidelberg, 2016, ISBN 9783662490945.

[25] L. Duan, L. Hou, T. W. Lee, J. Qiao, D. Zhang, G. Dong, L. Wang, and Y. Qiu: *Solution processable small molecules for organic light-emitting diodes.* J. Mater. Chem., 20:6392–6407, 2010. doi 10.1039/B926348A.

[26] R. H. Friend, R. W. Gymer, A. B. Holmes, J. H. Burroughes, R. N. Marks, C. Taliani, D. D. C. Bradley, D. A. Dos Santos, J. L. Brédas, M. Lögdlund, and W. R. Salaneck: *Electroluminescence in conjugated polymers.* Nature, 397:121–128, 1999. doi 10.1038/16393.

[27] G. Hadziioannou and P. F. van Hutten: *Semiconducting Polymers: Chemistry, Physics and Engineering.* Wiley-VCH, Weinheim, 2000, ISBN 3527295070.

[28] W. Knoll and R. C. Advincula: *Functional Polymer Films.* Wiley-VCH, Weinheim, 2011, ISBN 9783527321902.

[29] N. Koch: *Organic Electronic Devices and Their Functional Interfaces.* ChemPhysChem, 8:1438–1455, 2007. doi 10.1002/cphc.200700177.

[30] J. Shinar and R. Shinar: *Organic light-emitting devices (OLEDs) and OLED-based chemical and biological sensors: an overview.* J. Phys. D: Appl. Phys., 41:133001, 2008. doi 10.1088/0022-3727/41/13/133001.

[31] S. Ogawa: *Organic Electronics Materials and Devices.* Springer Japan, Tokyo, 2015, ISBN 9784431556541.

[32] S. Schols: *Device Architecture and Materials for Organic Light-Emitting Devices.* Springer, Dordrecht, 2011, ISBN 9789400716070.

[33] H. Bässler: *Charge Transport in Disordered Organic Photoconductors a Monte Carlo Simulation Study.* Phys. Status Solidi B, 175:15–56, 1993. doi 10.1002/pssb.2221750102.

[34] M. Schwoerer and H. C. Wolf: *Organic Molecular Solids.* Wiley-VCH, Weinheim, 2007, ISBN 9783527405404.

[35] J. P. Dakin and R. G. W. Brown: *Handbook of Optoelectronics (Two-Volume Set).* Taylor & Francis, Bristol, 2006, ISBN 0750306467.

[36] S. Kappaun, C. Slugovc, and E. J. W. List: *Phosphorescent Organic Light-Emitting Devices: Working Principle and Iridium Based Emitter Materials.* Int. J. Mol. Sci., 9:1527–1547, 2008. doi 10.3390/ijms9081527.

[37] J. S. Wilson, A. S. Dhoot, A. J. A. B. Seeley, M. S. Khan, A. Köhler, and R. H. Friend: *Spin-dependent exciton formation in π-conjugated compounds.* Nature, 413:828–831, 2001. doi 10.1038/35101565.

[38] S. Ho, S. Liu, Y. Chen, and F. So: *Review of recent progress in multilayer solution-processed organic light-emitting diodes.* J. Photon. Energy, 5:057611–1–057611–17, 2015. doi 10.1117/1.JPE.5.057611.

[39] Z. Hu, K. Zhang, F. Huang, and Y. Cao: *Water/alcohol soluble conjugated polymers for the interface engineering of highly efficient polymer light-emitting diodes and polymer solar cells.* Chem. Commun., 51:5572–5585, 2015. doi 10.1039/C4CC09433F.

[40] N. C. Greenham, R. H. Friend, and D. D. C. Bradley: *Angular Dependence of the Emission from a Conjugated Polymer Light-Emitting Diode: Implications for efficiency calculations.* Adv. Mater., 6:491–494, 1994. doi 10.1002/adma.19940060612.

[41] W. Brütting, J. Frischeisen, T. D. Schmidt, B. J. Scholz, and C. Mayr: *Device efficiency of organic light-emitting diodes: Progress by improved light outcoupling.* Phys. Status Solidi A, 210:44–65, 2013. doi 10.1002/pssa.201228320.

[42] J. I. Goldstein, D. E. Newbury, J. R. Michael, N. W.M. Ritchie, J. H. J. Scott, and D. C. Joy: *Scanning Electron Microscopy and X-Ray Microanalysis.* Springer, New York, 2018, ISBN 9781493966745.

[43] D. B. Williams and C. B. Carter: *Transmission Electron Microscopy: A Textbook for Materials Science.* Springer, Boston, 2009, ISBN 9780387765013.

[44] P. Hawkes and J. C. H. Spence: *Science of Microscopy.* Springer, New York, 2007, ISBN 9780387252964.

[45] R. F. Egerton: *Physical Principles of Electron Microscopy: An Introduction to TEM, SEM, and AEM.* Springer, New York, 2005, ISBN 9780387258003.

[46] J. M. Zuo and J. C. H. Spence: *Advanced Transmission Electron Microscopy.* Springer, New York, 2017, ISBN 9781493966059.

[47] L. A. Giannuzzi and F. A. Stevie: *Introduction to Focused Ion Beams: Instrumentation, Theory, Techniques and Practice.* Springer, Boston, 2005, ISBN 9780387233130.

[48] Z. M. Wang: *FIB Nanostructures.* Springer, Cham, 2013, ISBN 9783319028736.

[49] R. Jenkins, R. Manne, R. Robin, and C. Senemaud: *IUPAC-nomenclature system for X-ray spectroscopy.* X-Ray Spectrom., 20:149–155, 1991. doi 10.1002/xrs.1300200308.

[50] L. Reimer and H. Kohl: *Transmission Electron Microscopy.* Springer, New York, 2008, ISBN 9780387400938.

[51] P. Wobrauschek: *Total reflection X-ray fluorescence analysis - a review.* X-Ray Spectrom., 36:289–300, 2007. doi 10.1002/xrs.985.

[52] D. K. G. de Boer, A. J. G. Leenaers, and W. W. van den Hoogenhof: *Glancing-incidence x-ray analysis of thin-layered materials: A review.* X-Ray Spectrom., 24:91–102, 1995. doi 10.1002/xrs.1300240304.

[53] K. N. Stoev and K. Sakurai: *Review on grazing incidence X-ray spectrometry and reflectometry.* Spectrochim. Acta B, 54:41–82, 1999. doi 10.1016/S0584-8547(98)00160-8.

[54] R. Klockenkämper and A. von Bohlen: *Total-Reflection X-Ray Fluorescence Analysis and Related Methods.* Wiley-Blackwell, Hoboken, 2014, ISBN 9781118985953.

[55] W. W. Van Den Hoogenhof and D. K. G. De Boer: *Glancing-incidence X-ray analysis.* Spectrochim. Acta B, 48:277–284, 1993. doi 10.1016/0584-8547(93)80034-R.

[56] D. K. Bowen and B. K. Tanner: *Characterization of engineering surfaces by grazing-incidence X-ray reflectivity.* Nanotechnology, 4:175, 1993. doi 10.1088/0957-4484/4/4/001.

[57] D. K. G. de Boer: *Glancing-incidence x-ray fluorescence of layered materials.* Phys. Rev. B, 44:498–511, 1991. doi 10.1103/PhysRevB.44.498.

[58] M. K. Tiwari, G. S. Lodha, and K. J. S. Sawhney: *Applications of the 'CAT-GIXRF' computer program to the grazing incidence X-ray fluorescence and X-ray reflectivity characterization of thin films and surfaces.* X-Ray Spectrom., 39:127–134, 2010. doi 10.1002/xrs.1215.

[59] D. Ingerle, M. Schiebl, C. Streli, and P. Wobrauschek: *Combination of grazing incidence x-ray fluorescence with x-ray reflectivity in one table-top spectrometer for improved characterization of thin layer and implants on/in silicon wafers.* Rev. Sci. Instrum., 85:083110, 2014. doi 10.1063/1.4893383.

[60] D. Ingerle, F. Meirer, G. Pepponi, E. Demenev, D. Giubertoni, P. Wobrauschek, and C. Streli: *Combined evaluation of grazing incidence X-ray fluorescence and X-ray reflectivity data for improved profiling of ultra-shallow depth distributions.* Spectrochim. Acta B, 99:121–128, 2014. doi 10.1016/j.sab.2014.06.019.

[61] P. van der Heide: *X-Ray Photoelectron Spectroscopy: An Introduction to Principles and Practices.* Wiley, Hoboken, 2012, ISBN 9781118062531.

[62] H. R. Verma: *Atomic and Nuclear Analytical Methods.* Springer, Berlin, 2007, ISBN 9781118062531.

[63] J. C. Vickerman and I. S. Gilmore: *Surface Analysis – The Principal Techniques.* Wiley, Chichester, 2009, ISBN 9780470017630.

[64] R. F. Egerton: *Control of radiation damage in the TEM.* Ultramicroscopy, 127:100–108, 2013. doi 10.1016/j.ultramic.2012.07.006.

[65] A. Armigliato, S. Frabboni, G. C. Gazzadi, and R. Rosa: *FIB Preparation of a NiO Wedge-Lamella and STEM X-Ray Microanalysis for the Determination of the Experimental k(O-Ni) Cliff-Lorimer Coefficient.* Micros. Microanal., 19:79–84, 2013. doi 10.1017/S1431927612013876.

[66] P. van Espen, H. Nullens, and F. Adams: *A computer analysis of X-ray fluorescence spectra.* Nuc. Instr. and Meth., 142:243–250, 1977. doi 10.1016/0029-554X(77)90834-5.

[67] B. Vekemans, K. Janssens, L. Vincze, F. Adams, and P. Van Espen: *Analysis of X-ray spectra by iterative least squares (AXIL): New developments.* X-Ray Spectrom., 23:278–285, 1994. doi 10.1002/xrs.1300230609.

[68] XRF Group International Atomic Energy Agency Laboratories Seibersdorf: *Quantitative X-ray analysis system User's manual and guide to X ray fluorescence technique.* International Atomic Energy Agency (IAEA), Seibersdorf, 2009.

[69] S. Smolek: *Entwicklung eines energiedispersiven Mikro-Röntgenfluoreszenzspektrometers zur Analyse leichter Elemente.* TU Wien, 2014.

[70] R. Van Grieken and A. Markowicz: *Handbook of X-Ray Spectrometry, Second Edition.* Practical Spectroscopy. Taylor & Francis, Abingdon, 2002, ISBN 9780824706005.

[71] C. Streli, H. Aiginger, and P. Wobrauschek: *Total reflection X-ray fluorescence analysis of low-Z elements.* Spectrochim. Acta B, 44:491–497, 1989. doi 10.1016/0584-8547(89)80055-2.

[72] C. Streli, P. Wobrauschek, B. Beckhoff, G. Ulm, L. Fabry, and S. Pahlke: *First results of TXRF measurements of low-Z elements on Si wafer surfaces at the PTB plane grating monochromator beamline for undulator radiation at BESSY II.* X-Ray Spectrom., 30:24–31, 2001. doi 10.1002/xrs.463.

[73] C. Streli, G. Pepponi, P. Wobrauschek, B. Beckhoff, G. Ulm, S. Pahlke, L. Fabry, T. Ehmann, B. Kanngießer, W. Malzer, and W. Jark: *Analysis of low Z elements on Si wafer surfaces with undulator radiation induced total reflection X-ray fluorescence at the PTB beamline at BESSY II.* Spectrochim. Acta B, 58:2113–2121, 2003. doi 10.1016/j.sab.2003.05.008.

[74] P. Hönicke, B. Beckhoff, M. Kolbe, D. Giubertoni, J. van den Berg, and G. Pepponi: *Depth profile characterization of ultra shallow junction implants.* Anal. Bioanal. Chem., 396:2825–2832, 2010. doi 10.1007/s00216-009-3266-y.

[75] P. Hönicke, I. Holfelder, M. Kolbe, J. Lubeck, B. Pollakowski-Herrmann, R. Unterumsberger, J. Weser, and B. Beckhoff: *Determination of SiO2 and C layers on a monocrystalline silicon sphere by reference-free x-ray fluorescence analysis.* Metrologia, 54:481–486, 2017. doi 10.1088/1681-7575/aa765f.

[76] D. Ingerle, G. Pepponi, F. Meirer, P. Wobrauschek, and C. Streli: *JGIXA - A software package for the calculation and fitting of grazing incidence X-ray fluorescence and X-ray reflectivity data for the characterization of nanometer-layers and ultra-shallow-implants.* Spectrochim. Acta B, 118:20–28, 2016. doi 10.1016/j.sab.2016.02.010.

[77] D. B. Asay and S. H. Kim: *Evolution of the Adsorbed Water Layer Structure on Silicon Oxide at Room Temperature.* J. Phys. Chem. B, 109:16760–16763, 2005. doi 10.1021/jp053042o.

[78] D. K. Bowen and B. K. Tanner: *X-Ray Metrology in Semiconductor Manufacturing.* CRC, Boca Raton, 2006, ISBN 9780849339288.

[79] M. Rauwolf, C. Vanhoof, K. Tirez, E. Maes, D. Ingerle, P. Wobrauschek, and C. Streli: *Total reflection X-ray fluorescence measurements of S and P in proteins using a vacuum chamber specially designed for low Z elements.* Spectrochim. Acta B, 101:118–122, 2014. doi 10.1016/j.sab.2014.07.022.

[80] D. Wang, Z. Wu, X. Zhang, B. Jiao, S. Liang, D. Wang, R. He, and X. Hou: *Solution-processed organic films of multiple small-molecules and white light-emitting diodes.* Org. Electron., 11:641–648, 2010. doi 10.1016/j.orgel.2010.01.004.

[81] K. S. Yook and J. Y. Lee: *Small Molecule Host Materials for Solution Processed Phosphorescent Organic Light-Emitting Diodes.* Adv. Mater., 26:4218–4233, 2014. doi 10.1002/adma.201306266.

[82] A. R. G. Smith, K. H. Lee, A. Nelson, M. James, P. L. Burn, and I. R. Gentle: *Diffusion – the Hidden Menace in Organic Optoelectronic Devices.* Adv. Mater., 24:822–826, 2012. 10.1002/adma.201104029.

[83] S. Lee, J. H. Kang, D. A. Ahn, H. K. Shon, T. G. Lee, S. Park, M. C. Suh, and Y. Park: *Sputter Depth-Profile Study of Accelerated Interface Mixing by Thermal Annealing in Solution-Processed Organic Light-Emitting Diodes.* Adv. Mater. Interfaces, 6:1801627, 2019. doi 10.1002/admi.201801627.

[84] Y. Yu, Z. Wu, L. He, B. Jiao, and X. Hou: *A solvent/non-solvent system for achieving solution-processed multilayer organic light-emitting devices.* Thin Solid Films, 589:852–856, 2015. doi 10.1016/j.tsf.2015.07.043.

[85] S. Ho, Y. Chen, S. Liu, C. Peng, D. Zhao, and F. So: *Interface Effect on Efficiency Loss in Organic Light Emitting Diodes with Solution Processed Emitting Layers.* Adv. Mater. Interfaces, 3:1600320, 2016. doi 10.1002/admi.201600320.

[86] S. Scholz, D. Kondakov, B. Lüssem, and K. Leo: *Degradation Mechanisms and Reactions in Organic Light-Emitting Devices.* Chem. Rev., 115:8449–8503, 2015. doi 10.1021/cr400704v.

List of Figures

List of Tables

List of Acronyms

Al	aluminum
Ar	argon
Au	gold
AXIL	analysis of X-ray spectra by iterative least squares
BF	bright field
BSE	backscattered electron
C	carbon
CCD	charge-coupled device
CCS	cleaning cross section
Cu	copper
EDX	energy dispersive X-ray spectroscopy
EL	electroluminescence
EML	emission layer
ETL	electron transport layer
ETM	electron transport material
FIB	focused ion beam
Ga	gallium
GIS	gas injection system
GIXRF	grazing incidence X-ray fluorescence
HIL	hole injection layer
HOMO	highest occupied molecular orbital
HTL	hole transport layer
HTM	hole transport material
In	indium
IQE	internal quantum efficiency
Ir	iridium
Ir(ppy)$_3$	tris(2-phenylpyridine)iridium(III)

ITO	indium tin oxide
JGIXA	Java grazing incidence X-ray analysis
Liq	lithium 8-quinolate
LUMO	lowest unoccupied molecular orbital
Mg	magnesium
MM	micromanipulator
N	nitrogen
O	oxygen
OLED	organic light-emitting diode
PEDOT:PSS	poly(3,4-ethylenedioxythiophene) polystyrene sulfonate
Pt	platinum
RCS	regular cross section
S	sulfur
SDD	silicon drift detector
SE	secondary electron
SEM	scanning electron microscope
Si	silicon
$\mathbf{SiO_2}$	silicon dioxide
SM	small molecule
STEM	scanning transmission electron microscope
TEM	transmission electron microscope
Ti	titanium
TXRF	total reflection X-ray fluorescence
W	tungsten
XPS	X-ray photoelectron spectroscopy
XRF	X-ray fluorescence
XRR	X-ray reflectometry
XSW	X-ray standing wave
Z	atomic number

Publications

Parts of this thesis have been published in the following articles:

- A. Maderitsch, D. Ingerle, T. Bretschneider, M. Rauwolf, C. Pflumm, H. Buchholz, H. Borchert, C. Streli, and J. Parisi: *Analysis of organic multi-layer structures using a combined grazing incidence X-ray fluorescence/X-ray reflectometry approach.* Spectrochim. Acta B, 148:188-192, 2018. doi 10.1016/j.sab.2018.07.006
- A. Maderitsch, C. Pflumm, H. Buchholz, H. Borchert, and J. Parisi: *The impact of the deposition process of the emitting layer on the internal structure of organic light-emitting diodes.* J. Phys. D: Appl. Phys., 52:455105, 2019. doi 10.1088/1361-6463/ab375a.

Acknowledgments

I want to thank all people, which supported me in any form during the work on this thesis.

In the first place, I want to thank Prof. Dr. Jürgen Parisi for providing me the opportunity to work within his research group and the fruitful discussions.

Secondly, I want to thank Dr. Holger Borchert for supervising during the work for this thesis and providing suggestions and critique.

I want to thank Merck KGaA for funding the project and providing samples, Dr. Christof Pflumm and Dr. Herwig Buchholz for their support.

I also want to express my gratitude to the members of the Energy and Semiconductor research laboratory at the Carl von Ossietzky University Oldenburg, especially Matthias Macke, Holger Koch and Marion Luttmann for their help in the laboratories and with the equipment and my colleagues and friends Alexandra Erdt and Dr. Oliya Abdullaeva, who supported me on and off the campus.

I appreciate the support with administrative matters from Elzbieta Chojnowski and Grit Schürmann.

For introducing me to the transmission electron microscopes I want to thank Dr. Erhard Rhiel. I also appreciate the help from Edith Kieselhorst and Ute Friedrich.

I want to thank the radiation physics department at Atominstitut, TU Wien: Prof. Dr. Christina Streli and Prof. Dr. Peter Wobrauschek for cooperating on this project, Dr. Dieter Ingerle for performing the GIXRF/XRR measurements and the introduction to his software JGIXA, Dr. Mirjam Rauwolf for the TXRF measurements.

Special thanks to DI Stephan Smolek for helping me adapt his software tools for data handling and evaluation and his continuous moral support.

Finally, I want to thank Günther and my family for their patience.

Erklärung

Hiermit erkläre ich, dass ich die Arbeit selbstständig verfasst und nur die angegebenen Hilfsmittel benutzt habe.

Friedrichsdorf, am 12.08.2019 ____________________________________
Angelika Maderitsch